



Defect characteristics and analysis of their variability in metal L-PBF additive manufacturing

Niloofar Sanaei^a, Ali Fatemi^{a,b,*}, Nam Phan^c

^a Department of Mechanical, Industrial and Manufacturing Engineering, University of Toledo, Toledo, OH, United States

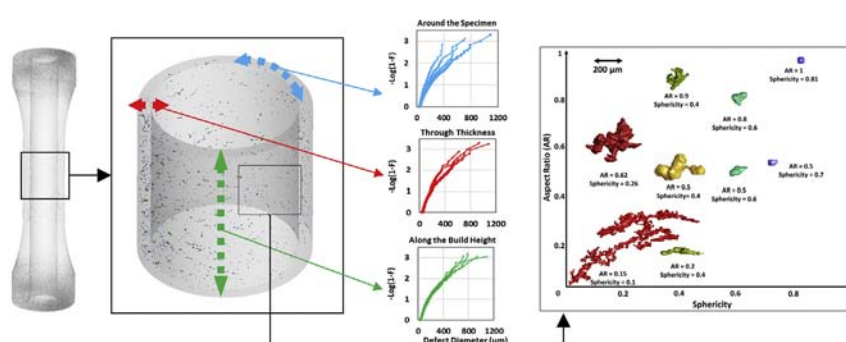
^b Department of Mechanical Engineering, University of Memphis, Memphis, TN, United States

^c Structures Division, US Naval Air Systems Command, Patuxent River, MD, United States

HIGHLIGHTS

- Variability analysis of defect distributions of L-PBF specimens showed critical defects concentrated in specific locations.
- Apt process parameters, surface machining, and Hot Isostatic Pressing improved defect content repeatability in specimens.
- Hot Isostatic Pressing increased defects aspect ratio and decreased their size, therefore reduced directionality of defects.
- Lack of Fusion defects decreased 2D analysis results reliability and increased the need for 3D defect analysis.

GRAPHICAL ABSTRACT



ARTICLE INFO

Article history:

Received 13 June 2019

Received in revised form 28 July 2019

Accepted 31 July 2019

Available online 05 August 2019

Keywords:

Additive manufacturing

Defect characterization

Computed tomography

Defect variability

Ti-6Al-4V

17-4 PH stainless steel

Data availability:

The raw/processed data required to reproduce these findings cannot be shared at this time as the data also forms part of an ongoing study.

ABSTRACT

Additive manufacturing (AM) has provided an opportunity for fabricating complex parts. Fabricating these parts without defects is currently a challenge. Therefore, understanding AM defects is fundamental to the structural integrity of load carrying components, failure analysis, and defect-based modeling of mechanical performance. This work investigates defect content of metal AM specimens and correlations between defect characteristics (size, sphericity/circularity, aspect ratio) using 2D and 3D defect characterization techniques. Distributions of defect characteristics based on location throughout AM specimens were analyzed and the variabilities of defect characteristics within these specimens were studied. Laser-Based Power Bed Fusion (L-PBF) specimens manufactured with different metals, different AM machines and built directions, different surface conditions, and different thicknesses were evaluated. Significant variability in defect characteristics based on location, especially in as-built surface specimens was observed. Well-optimized process parameters and post-processing reduced the overall volume fraction of defects, and the specified variabilities, and resulted in a more random dispersion of defects around the specimens. 2D and 3D defect analysis showed similar trends regarding correlations between defect characteristics and provided complementary information about the actual defect content based on their resolution.

© 2019 The Authors. Published by Elsevier Ltd. This is an open access article under the CC BY-NC-ND license (<http://creativecommons.org/licenses/by-nc-nd/4.0/>).

Abbreviations: AM, additive manufacturing; AR, aspect ratio; CT, computed tomography; EBM, electron beam melting; HIP, Hot Isostatic Pressing; K-S, Kolmogorov-Smirnov; LOF, Lack of Fusion; L-PBF, Laser-Based Power Bed Fusion; PBF, Powder Bed Fusion; ROI, Region of Interest; SEM, Scanning Electron Microscopy; SLM, selective laser melting; SRμT, Synchrotron Radiation Micro-Tomography; 2D, two dimensional; 3D, three dimensional.

* Corresponding author at: Department of Mechanical Engineering, University of Memphis, Memphis, TN, United States.

E-mail address: afatemi@memphis.edu (A. Fatemi).

<https://doi.org/10.1016/j.matdes.2019.108091>

0264-1275/© 2019 The Authors. Published by Elsevier Ltd. This is an open access article under the CC BY-NC-ND license (<http://creativecommons.org/licenses/by-nc-nd/4.0/>).

Nomenclature

D	distance between empirical distribution functions
E_a	energy density
E_1, E_2	empirical distribution functions
F	cumulative distribution function
h	hatch spacing or line offset
t	layer thickness
P	beam power
α	significance factor
v	beam velocity

1. Introduction

Additive manufacturing (AM) methods have been flourishing in the last decade for production of unique, critical, and geometrically complex parts and structures. Despite the promising results achieved in terms of material and mechanical properties, quality control and variability in mechanical properties as a result of variability in microstructure and defect characteristics is still an ongoing challenge [1]. With current AM technology even in case of optimized process parameters, defects still occur and can potentially lead to failures of AM parts, particularly in fatigue critical applications. Therefore, standardized test procedures to gain non-destructive insights into the quality of AM parts are being developed [2].

Safety-critical components made by AM, such as in biomedical and aerospace applications, should be reliable to operate under a wide range of loading conditions, from static to complex dynamic mechanical loadings in harsh environmental conditions. These components should have proper mechanical properties and particularly fatigue performance which is significantly affected by material defects. Robust techniques and analysis methodologies are needed for detection and characterization of AM defects for these safety-critical parts and components of high value.

Powder Bed Fusion (PBF) is currently the most commonly used AM technique. Two main power sources used in PBF are lasers and electron beams. Specimens in this study were manufactured by L-PBF machines. Ti-6Al-4V and 17-4 PH were used here for presentation of the methods, and ideas, although the performed statistical analyses may also be used for other materials with similar defect structures. Ti-6Al-4V is of specific interest due to its high strength, light weight, biocompatibility, and corrosion resistance. 17-4 PH stainless steel is an alloy commonly used in medical sectors, chemical industries, commercial applications, and defense.

Wrought Ti-6Al-4V has been reported as a dual-phase material with equiaxed $\alpha + \beta$ grains or lamellar $\alpha + \beta$ colonies interspersed between nearly equiaxed α grains. However, a martensitic acicular α' microstructure for as-built SLM (Selective Laser Melted) specimens is usually observed [3–6]. During heat treatment of SLM Ti-6Al-4V, based on temperature and time, a gradual decomposing of the martensitic phase to a mixture of α and β fine needles is observed. Increasing the temperature leads to coarsening of the microstructure along with the formation of lamellar ($\alpha + \beta$) and globular α at prior- β grain boundaries. Thus, microstructure of HIPed (Hot Isostatic Pressed) specimens comprised of long and wide columnar grains and has been reported to be relatively similar to the wrought reference material in most cases [7,8]. Less or no martensitic structure is reported for EBM (Electron Beam Melted) samples compared to SLM samples mostly due to higher base plate temperature during the process, and the presence of fine lamellar α - β microstructure in as-built EBM samples has been confirmed [9].

For non-heat treated SLM 17-4 PH, very fine parallel columnar austenitic grains have been observed, which have shown strongly preferred orientation since the grains grow along the heat transfer directions, both perpendicular and parallel to build direction [10]. Microstructure

and phase composition of SLM 17-4 PH vary based on powder composition, SLM conditions, and heat treatment; and may be very different from conventionally manufactured 17-4 PH.

AM metals have shown finer microstructure compared to wrought counterparts [3]. Also, since defects generally have a less pronounced effect under static loading, AM metals generally show good static strength. However, AM microstructural characteristics and the existence of defects typically lead to lower ductility and lower fracture toughness [11]. Since fatigue is a local phenomenon, resistance to fatigue failure is greatly influenced by the existence of defects. Fatigue cracks usually start at stress concentrations like pores and inclusions [12], and AM intrinsic defects such as Lack of Fusion (LOF) defects and gas porosities highly affect fatigue life [13]. Defects intrinsic to metal AM processes could also rise from accumulated residual stresses in the part during the manufacturing process and the resultant distortion [14]. Surface or near-surface defects specifically, could negatively affect the resistance of the metal to corrosion [15].

Predictability of the final defect content of AM parts is low. Raw powder manufacturing process, process variations in the production chamber, and post-processing treatments all affect the final defect content [16]. Therefore, characterization of defects is important for qualifying and quantifying the mechanical properties of AM parts. A clear picture of the distribution of the defects and their characteristics in an AM part should be obtained, and the trends that these distributions follow should be examined. This information can then be used towards process optimization approaches, necessary post-processing treatments, performance prediction, and for monitoring, maintenance, and replacement plans.

AM defects could also vary based on scanning strategy and their location in a component. Variation in the porosity of an AM part has been observed even based on its location in the chamber during build [17]. Components built with AM could have complex geometries containing sections with different thicknesses and varying build orientations which could affect the distribution of defects. Variability in defect distributions might cause regions in the parts with accumulation of more detrimental defects. Such information is useful for probabilistic assessment of the fatigue performance of the parts based on distribution of critical defects.

2. Defect formation and characterization in metal AM

The mechanisms of formation of AM defects have been under investigation in recent years. Several publications have discussed various types of defects in metal AM and described the mechanism of their formation. The focus of this paper is on defects of L-PBF metals. However, the analysis techniques could also apply to all other AM process defects. These defects are induced to the AM parts during the manufacturing process. The localized heating and rapid cooling along with consuming powdered material as the feedstock create a favorable environment for defect formation by leaving small cracks, un-melted particles, LOF regions, or creating gas bubbles. Examples of these defects which highly depend on the process parameters and material can be seen in Fig. 1 for two different materials and manufacturing machines discussed in this work.

The feedstock material can be the first source of defect formation based on its atomization process and whether it carries a high amount of entrapped gas. The energy input is another main source for defect formation which should be optimized based on the material and other process parameters to maintain a low defect producing process. The energy density per unit volume (E_a) is a parameter commonly used in laser-based metal AM to describe local heat input per unit volume and compare the effect of process parameters on defect content [18,19]. This parameter incorporates the beam speed, power, and offset between melt tracks and has shown to be useful for comparing various samples, or various locations within a build. It is given by:

$$E_a = \frac{P}{v \cdot h \cdot t} \text{ (J.mm}^{-3}\text{)} \quad (1)$$

where P , v , h , and t are the beam power (W), beam velocity (mm/s), hatch spacing or line offset (mm) which is the spacing between melt tracks, and layer thickness (mm), respectively. The energy supplied to the melt pool should be optimized to only partially melt the previously deposited layer in order to create a perfect bond between the two sequential layers. Any deviation from this optimized amount of energy could create insufficient melting or vaporization and a highly unstable melt pool [20–22].

Having insufficient energy will cause compromised bonding between layers and create LOF defects. These defects usually have sharp edges and are elongated between the layers and also laser tracks. Generally, large LOF defects are formed around and contain un-melted power particles. Having excess energy, on the other hand, will cause violent convection currents and significant vapor recoil forces, which can lead to ejected spatter and instability [23]. This can lead to the formation of voids and/or gas bubbles in the melt pool, which are generally spherical in shape due to the dominance of surface tension in the liquid metal. The entrapped gas content of these pores depends on whether a shielding gas was used, the type of feedstock powder, and the original gas entrapped in the powder particles. These gas pores might be hard to remove by post-processing treatment depending on the solubility of the contained gas [24].

Round pores are also formed when the high applied energy causes the melt to vaporize locally and become entrapped in the melt pool. Due to re-melting while depositing the next layer, there is a possibility for gas bubbles created on top of the melt pool to scape as opposed to the gas bubbles deeper in the melt pool which makes them more detrimental. High power and low scan speed strategy should be avoided to prevent the formation of these detrimental defects. This kind of porosity is sometimes referred to as keyhole induced porosity [25].

The characteristics of AM defects such as type, location, shape, size, orientation, and density are greatly influenced by the process parameters. These defects can be minimized during the process by optimization of manufacturing parameters such as powder characteristics, energy input, scanning speed, scanning strategy, build direction, layer thickness, and hatch spacing. Post-processing thermo-mechanical treatments such as HIPing, and surface treatments, might further reduce

these defects but they may not be fully eliminated. Preheating and keeping the base plate at a certain temperature during the process as well as appropriate cooling rates may also slightly influence the final defect content.

Thermo-mechanical processes such as stress relieving, annealing at various temperatures with various cooling rates, Hot Isostatic Pressing (HIP), and surface treatments such as surface machining, shot peening, or surface coating are usually performed on AM manufactured parts to improve the microstructure, internal defects and, surface defects. Heat treatment has shown not to significantly influence porosity content. However, HIPing is a method used for reducing the amount and size of the defects significantly and improves the microstructure, ductility, flexural modulus, fatigue strength, and fatigue crack initiation properties of the AM components [3,4,26]. It involves the simultaneous application of high temperatures and pressures to a component, in an inert gas atmosphere. The high temperature causes reduced yield stress and higher diffusion rates, and the applied pressure leads to small scale plastic flow, material transport, and pore collapse [27]. Characterization and control of process-related defects and anomalies and their impact on part durability is one of the main areas of concern that must be rigorously addressed for qualification and certification of AM parts [1]. Variability in AM machines, beam source/material interactions, and geometry can cause inconsistency in the microstructure and defects, and consequently variability in the mechanical performance even for the same processing conditions.

Characteristics of defects such as size (volume, area, diameter), shape, location, and distribution have shown to play key roles in mechanical properties and specifically fatigue performance of the AM metals and should be thoroughly studied in order to evaluate and quantify their effect. Quantitative characterization of spatial distribution and morphology of AM intrinsic defects might be difficult to achieve only by traditional methods of cross-section analysis or bulk density. Since the parts manufactured by AM process are relatively expensive, the non-destructive methods of defect characterization such as the Archimedes method, gas pycnometry, and X-ray micro-CT are of great interest.

A study comparing these methods demonstrated that Archimedes and micro-CT with a voxel size of $\sim 9 \mu\text{m}$ result in comparable trends

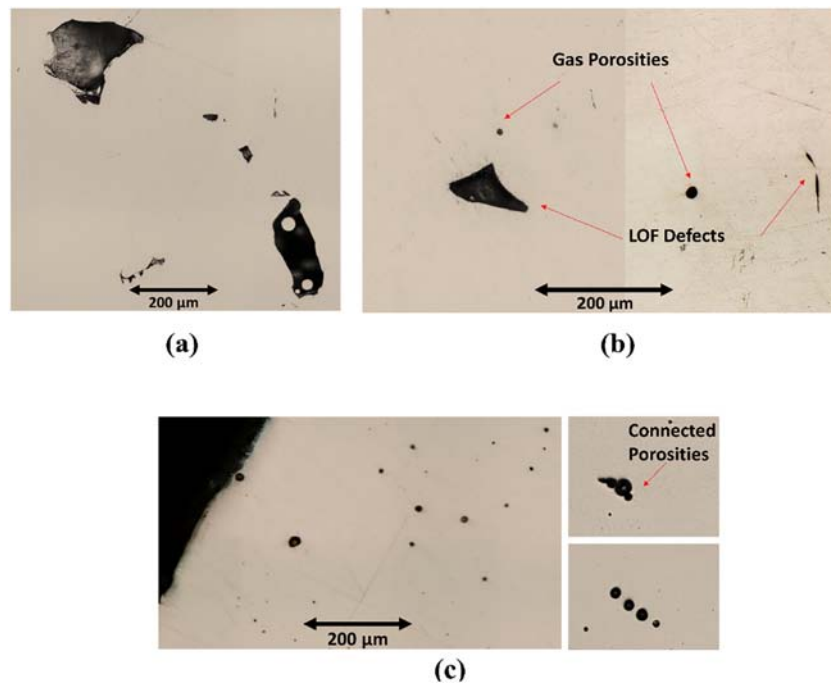


Fig. 1. (a) Irregular shape LOF defects and LOF defects containing un-melted particles on a polished surface of an AM250 Ti-6Al-4V specimen, (b) fewer and smaller irregular shape LOF defects and small gas porosities on a polished surface of a M290 Ti-6Al-4V specimen, (c) high number of small round gas porosities and occasional series of connected gas porosities on a polished surface of a M290 17-4 PH specimen.

for the volume fraction of porosity in various samples [28]. However, the actual values slightly differ with the Archimedes method consistently generating lower values. They observed that gas pycnometry was not accurate enough for testing parts with porosity percentages lower than 0.5%, while the less expensive Archimedes method was adequate for inspecting volume fraction of porosity for parts in small series for identifying poor quality parts [28]. Another work also observed similar trends for the percentage of porosity from the Archimedes method and micro-CT with a voxel size of $\sim 2.5 \mu\text{m}$, but the Archimedes method values were not consistently lower than micro-CT [29].

Archimedes method and gas pycnometry are not capable of quantitatively providing any information on size, location, shape, or distribution of the defects. A high density ensures fewer pores as opposed to the lower density which is a sign of a higher number of pores. On the other hand, micro-CT has the potential to detect the defects in 3D space and provide information on defect volume, as well as location, morphology, and distribution of the defects which can also be useful to assess the effect of post-processing or mechanical testing on the defects. During X-ray micro-CT samples are irradiated with a beam of X-rays, the subsequent absorption X-ray image is measured, and such images are repeatedly acquired as the sample rotates [30].

Synchrotron Radiation Micro-Tomography (SR μ T) is also a method that has been used for defect characterization, monitoring, and measuring the in-situ formation of defects providing resolutions less than $1 \mu\text{m}$, and also for surface characterization in AM [31]. SR μ T, offers a new level of details in defect characterization, as the high-energy X-rays provide large penetration, a high signal to noise ratio, as well as the possibility of sub-micron voxel resolution.

Although 3D analysis results provide a wide variety of defect characteristics but might not be always available. 2D defect characterization can still provide valuable information on the defect content and can provide microscale details of the defects at a relatively low cost. A simple destructive method, such as cross-section analysis performed on an AM sample or a witness specimen built alongside the AM part using optical microscopy or Scanning Electron Microscopy (SEM), may be beneficial in terms of achieving high resolution and accuracy in measuring size, shape, and location of the microscopic defects. Although to achieve the required level of certainty for the observed results with only 2D characterization, multiple cross-sections might be necessary.

Based on the scanning resolution and the size of defects in 3D scanning, 2D analysis could also provide complementary insight such as the morphology of an irregular shape defect detected in 3D analysis, on aspects such as whether it is a LOF defect, contains un-melted particles, or it consists of a series of connected round gas porosities. The measured values by the software while processing micro-CT data could somewhat vary based on the resolution and the analysis parameters such as assumed contrast and local area size. This could result in measured defect area values higher or lower compared to microscopic methods.

In a study by Tammam-Williams et al. [19], micro-CT scans were performed over the whole volume of their simple cuboid EBM Ti-6Al-4V samples with a $9.9 \mu\text{m}$ voxel size, and also carried out on 1.6 mm machined sections from the sample edge and center with a voxel size of $2.1 \mu\text{m}$. They compared volume fraction of porosity gathered from the tomography data to equivalent volume distribution from conventional 2D optical microscopy using the Schwartz-Saltykov (S-S) analysis which is only applicable to spherical objects since the majority of their pores were spherical. After this transformation, their 2D and 3D results for the frequency of pores with sizes below $150 \mu\text{m}$ were in good agreement. Sections from planes parallel and perpendicular to build direction were used. They reported an average pore volume fraction of 0.2%.

Benefiting from 2D and 3D defect analysis, Kasperovich et al. [18] optimized the process parameters in their study with the goal of minimizing critical defects for SLM Ti-6Al-4V. To achieve high-resolution 3D results by synchrotron tomography, they extracted cylindrical specimens with 0.8 mm diameter and $\sim 7 \text{ mm}$ length from manufactured cuboids of $\sim 10 \times 10 \times 10 \text{ mm}^3$. They performed limited micro-CT scans

with a very high resolution and a voxel size of $(0.33 \mu\text{m})^3$. They also characterized the porosity content of each cuboid sample by 2D image analysis of metallographic longitudinal cross-sections parallel to the SLM building direction using three different parallel sections. Their 2D (surface fraction) and 3D (volume fraction) measurement results of the percent porosity were very close, one reason for which could be the very high resolution of the tomography. Their results showed two main categories of defects: circular/spherical defects created at excessive energy densities and elongated narrow defects formed by insufficient energy density. The fine ribbed surface of the first category of defects occurred due to the surface tension forces exerting shear on the liquid surface. The second group of defects was observed to be formed around un-melted particles and reported to be mainly perpendicular to the building direction.

Benedetti et al. [7] evaluated the porosity content of their Ti-6Al-4V ELI samples by 2D metallographic measurements using five different parallel sections perpendicular to the build direction and 3D micro-CT scan with a voxel size of $(2.8 \mu\text{m})^3$. Although they mention that generally the micro-CT scans tend to systematically estimate lower porosity than the metallographic inspections, their micro-CT measurements lie within the error band of their 2D analysis results. In their as-built solid cylindrical samples, they observed the highest porosity (about 0.35%) from both 2D and 3D methods as well as the largest defects to be located in the outermost 0.4 mm thick layer. HIPing effectively reduced porosity fraction throughout the samples to below 0.05%, while shot peening had only changed the shape rather than the volume of the pores located in the outermost layer.

Seifi et al. [11] studied the distribution of defects in EBM Ti-6Al-4V cuboid samples along the build height using micro-CT data with $25 \mu\text{m}$ voxel size. They evaluated the defect content of their samples in three sections along the build height at the start, the middle, and the end of the build and used statistical presentations to better visualize the correlation between the distribution of defects and their locations. They observed the greatest intensity of clustered defects at the outside walls of the build, the edges to possess a lower intensity of defects, with the core to be almost defect-free. Also, the middle section of a group of their samples showed a higher probability of defects than its end and a lower fracture toughness. They associated the change of the defect spatial distributions to the beam travel direction and also emphasized the potential role of the hatching pattern used during the build process.

The aims of this paper are to analyze the variability of defect characteristics based on defect location throughout the gage section of thin-wall tube specimens with a thickness of $\sim 1.2\text{--}1.5 \text{ mm}$ and grip section with a thickness of $\sim 6 \text{ mm}$. The specimens were built with three different L-PBF machines and their defects were characterized and analyzed by micro-CT, optical microscopy, and appropriate statistical methods. Correlations between various defect characteristics are presented and defect analysis results are compared based on the data obtained from micro-CT and optical metallography.

The goal is to provide a clear evaluation of the variability in the characteristics of the defects within specimens built with different materials, process parameters, build orientations, heat treatments, and surface conditions. The important factors that could influence the variability are discussed and the two characterization methods used are compared. The effect of these defects on fatigue behavior of AM metals is discussed in a comprehensive literature review by the authors.

3. Materials and methods

3.1. Materials and specimen fabrication

Two different materials, Ti-6Al-4V and 17-4 PH, were used in this study. Specimens characterized in this work were thin-walled tubular specimens, as can be seen in Fig. 2. These specimens were designed for multiaxial (axial-torsion) fatigue testing, the results of which were

discussed in previous publications [13,32], based on the ASTM Standard E2207 [33]. Two different L-PBF machines were used for fabricating the Ti-6Al-4V AM specimens. For the first group of specimens built with M290 machine, Extra-Low Interstitials (ELI) grade 23 Ti-6Al-4V powder with a particle size of 15–45 μm was used in accordance with ASTM Standard B348 [34]. The orientations of fabrication of the specimens were vertical and diagonal (45° relative to the base) and the specimens were built on a base plate. A Ti-6Al-4V specimen manufactured by another M290 machine with similar process parameters was also used for defect characterization and comparison to examine the repeatability of the defect content with two identical machines in the as-built condition.

L-PBF machine AM250 was used to build the second group of Ti-6Al-4V specimens, using gas-atomized grade 23 powder with a particle size of 15–45 μm . Specimens were fabricated vertically on a base plate using support structures with a thickness of 5 mm. The scanning strategy consisted of fabricating the supports, hatching, and two borders; a large border, followed by a second smaller border to smoothen the edges.

For manufacturing the 17-4 PH specimens, the L-PBF machine M290 with pre-alloyed argon-atomized 17-4 PH SS powder with the particle size distribution range of 15–45 μm was used. The mean volume diameter of the powder was 37.13 μm with a standard deviation of 9.85 μm . The orientation of fabrication of the specimens was vertical and the specimens were built on a base plate. The process parameters and conditions for each material are listed in Table 1.

Most of the Ti-6Al-4V AM specimens were annealed to relieve the residual stresses, inside a preheated chamber at 700 $^\circ\text{C}$ for 1 h under a constant supply of Argon gas and then air-cooled at room temperature. Several oversized specimens were built with larger dimensions and were later surface machined from inside and outside final dimensions and polished. A number of Ti-6Al-4V M290 specimens were HIPed in order to minimize the defects and improve the ductility, at 920 $^\circ\text{C}$ and 100 MPa for 3 h in accordance with ASTM Standard F2924 [35]. All 17-4 PH specimens had as-built surface and were heat treated. This heat treatment consisted of heating the specimens at 1050 $^\circ\text{C}$ for half an hour, air cooling at room temperature, followed by heating at 552 $^\circ\text{C}$ for 4 h, and then again air cooling to room temperature. The summary of material, processing and post-processing conditions, and final thicknesses of all the specimens can be found in Fig. 3.

3.2. 3D defect characterization: X-ray micro-CT

Results of micro-CT of 14 specimens were used for analysis in this study. Two different specimens for each condition were chosen randomly for analysis to study the repeatability of the results and variation between the results of two specimens from the same batch. The X-Ray micro-CT scanning and reconstruction were performed on the

specimens by a North Star Imaging Computed Tomography system. Setting of 100 kV for voltage of the microfocus X-ray source, operating at a current of 250 μA was used for each sample. Perkin Elmer detector with a pixel pitch of $400 \times 400 \mu\text{m}$ was used for the process.

All the 3D defect analysis on micro-CT results was performed using VGSTUDIO MAX 3.1 software. The process involved using surface determination tools, Region of Interest (ROI) selections, and porosity analysis using the custom method VGEasyPore. The software could generate data on defect size (volume, diameter, projected areas), position, sphericity, as well as the distance from the surface. Also, the defect projected area along the three principal directions and the projected sizes of the bounding box surrounding the defect were automatically determined. To ensure the rough surface does not interfere with the analysis of internal defects, the rough surface was removed by surface refinement in the software before defect analysis of 3D models with as-built surfaces. Advanced Surface Determination algorithm in the software defines the material boundary by locally adapted gray values. This is important for the complicated surface morphology of as-built AM metals since the same gray value will be interpreted differently depending on the surrounding voxels. During this process it is ensured that all internal voids and particles are removed and only the inner and outer surfaces of the specimens are recognized. The Erode/dilate algorithm is used next, which performs a morphological operation on the ROI and could expand or contract it. Using negative number of voxels based on the surface roughness of each specimen, ROI is contracted. This ensures that open pores and surface defects are not later considered in defect analysis.

The defects characteristics gathered from 3D analysis for which the variabilities were studied throughout the specimens include defect diameter, volume, projected area on three orthogonal planes (perpendicular and parallel to the build direction), sphericity, and aspect ratio. Defect diameter indicates the diameter of the circumscribed sphere of the defect and volume indicates the actual volume occupied by the defect. Defect sphericity is a measure of irregularity of the defect shape in 3D analysis and is equal to the ratio between the surface of a sphere with the same volume as the defect and the surface of the defect, which ranges between 0 and 1. A sphericity value of 1 represents a perfect sphere, while a value close to zero represents a highly irregular shape interconnected defect.

Defect aspect ratio is a measure of elongation of each defect defined as the ratio of the smallest projected size to the largest projected size of the bounding box surrounding the defect, ranging between 0 and 1 with lower values representing a more elongated defect. The analyzed projected area is the area of the projection of defect shape perpendicular to each axis.

A voxel size close to $(14 \mu\text{m})^3$ was achieved during micro-CT scanning by focusing on only a small part of the specimen gage section (15 mm length) and reducing the distance between the sample and

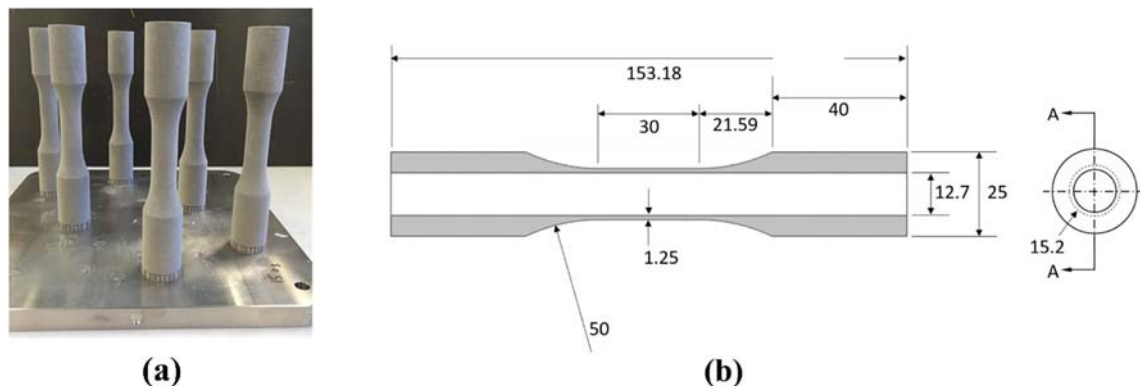


Fig. 2. (a) As-built thin-walled tubular specimens vertically manufactured by laser-based PBF machine (Courtesy of Dr. Shamsaei), (b) Detailed specimen geometry after surface machining.

Table 1
Build parameters used for specimen fabrication with laser-based PBF machines.

Specifications	Ti-6Al-4V		17-4 PH
	AM250	M290	M290
Powder	Grade 23 (ELI)	Grade 23 (ELI)	Argon-atomized
Powder size range (μm)	15–45	15–45	15–45
Laser power (W)	400	285	220
Scanning speed (mm/s)	1000	1200	756
Layer thickness (μm)	50	30	40
Hatch spacing (μm)	160	140	100
Hatch rotation (degree)	67	67	67
Energy density ($\text{J}\cdot\text{mm}^{-3}$)	50	56.4	72.7
Environment	Argon	Argon	Argon

the X-ray source. In other words, a smaller voxel size was reached by means of higher magnification. The voxel is a cube with the side equal to the corresponding size ($14\text{ }\mu\text{m}$). To stay away from resolution limits and noise particles, a cut-off threshold of $2 \times 2 \times 2$ (8) voxels as the volume of each detected defect was used in this study. The resolution is usually defined as the smallest feature perceptible from the reconstructed 3D voxel data [19]. A number of factors affect the resolution such as the large size of the part, blurring from a finite rather than point X-ray source, scatter of X-ray photons within the sample, beam hardening, mechanical errors from stage movement, and incorrect determination of the center of rotation during reconstruction [30].

3.3. 2D defect characterization: digital microscopy

A VHX-6000 series digital microscope capable of automatically stitching up to 200 pictures taken from the surface in magnification of $500\times$ was used in this work. For 2D characterization, horizontal cuts perpendicular to the specimen axis were made. After the specimens were sliced, the cut samples were mounted in a polymer mold. The

surfaces were ground and polished to get a flat face for uniform analysis conditions. The sample surfaces were ground on abrasive paper and cloth, starting from coarse grit and using progressively finer and finer grit sizes. The process was started from 240-grit SiC paper, went through 320-grit, 400-grit and was finished with 600-grit. This was followed by finer polish, Al_2O_3 suspension as recommended with abrasives with particle sizes of 0.3 mm and 0.05 mm. Samples were then cleaned with an ultrasonic cleaner and dried with pressurized air. Data collected from four sections from each specimen cut by EDM machine perpendicular to the specimen axis was used for comparisons. These cross-sections were cut from the micro-CT scanned gage section with a thickness of about 1.2 mm and from the thicker grip section of the same specimen with a thickness of about 6 mm for further comparisons.

After sample preparation, microscopy of the complete cross-section with high magnifications, and stitching the pictures together; size, shape, location, and local density of the defects were analyzed using ImageJ software. An ellipse was fit to each defect to represent the aspect ratio of each defect. Measurement results were checked for reliability and repeatability before the analysis. The defect characteristics gathered from the 2D analysis include defect feret diameter and area to represent defect size and circularity and aspect ratio to represent defect shape. Defect feret diameter is the longest distance between any two points along the defect selection boundary and defect area is the area of each defect within the outer selection boundary. Defect circularity is a measure of irregularity of the defect shape and is equal to 4π (area/perimeter²), which ranges between 0 and 1 with the circularity value of 1 representing a perfect circle.

The aspect ratio of the defect is a measure of elongation of each defect and is defined as the aspect ratio of the fitted ellipse to the defect, which is the value of minor axis over major axis or b/a , with values ranging between 0 and 1 and lower values representing more elongated defects.

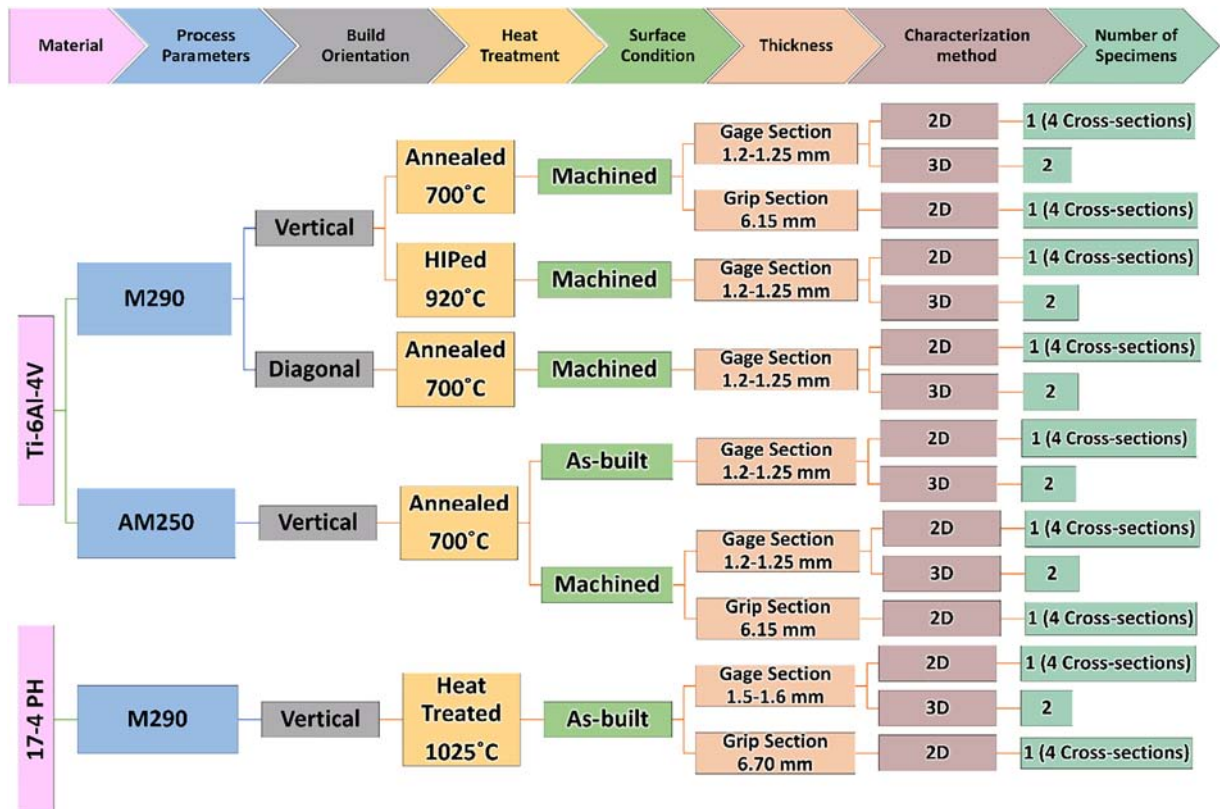


Fig. 3. Material, processing and post-processing conditions, thicknesses, and the number of Ti-6Al-4V and 17-4 PH specimens for which defect characteristics were analyzed.

3.4. Analysis of variability and comparison of distributions

Variability analysis results gathered from micro-CT of 14 specimens are presented in this study. The specimens for which defect characteristics were analyzed and the number of specimens characterized for each condition are presented in Fig. 3. The two AM machines had different sets of process parameters creating very different defect contents. All AM250 specimens considered here were vertically built and M290 specimens considered were vertically and diagonally built. Variabilities in the distributions of the defect characteristics gathered from 3D and 2D analysis results throughout the specimens were studied by statistical means.

The micro-CT scanned model was divided into various sections as shown in Fig. 4 and variability in distributions of the defect characteristics in these sections were compared. For 3D analysis, three different groups of distributions were considered. First, the scanned volume was divided into four equal control volumes sectioned along the build height, as shown in Fig. 4(a). The objectives were to examine the defect characteristics distributions along the height and recognize if there is significant variation and if this is the case, are these variations following a specific trend for all the specimens. Based on the observations discussed later, the defects were found to be randomly distributed along the height, so for the rest of the comparisons, the full height of the scanned volume was considered. The scanned volume was then divided into equal quadrants around the specimen axis as control volumes, as shown in Fig. 4(b). This was done to see if defects are randomly dispersed in the cross-section of the specimen around the axis of symmetry or if they are concentrated at specific locations around the specimen.

Finally, the scanned volume was divided into four shells with equal thicknesses, as shown in Fig. 4(c). This was performed by means of the known center of each defect, defined as the center position of the circumscribed sphere of the defect. The wall thickness consists of about 100 voxels which were divided into 4 smaller shells, each about 25 voxels thick. Each defect belonged to a shell if the center of that defect was located in that shell.

Generally, defects are not randomly distributed through thickness and there might be a difference between density and size of the defects based on their distance from the surface. This will help in choosing an appropriate control volume which is representative of the defect characteristics while characterizing defects for various purposes. Also, the spatial distribution of the defects could provide insight for in situ monitoring of the critical locations during the manufacturing process for any deviation from the optimized process parameters, and for investigating the effects of defects on mechanical performance, particularly fatigue.

To achieve a comprehensive perspective on the variabilities in defect characteristics while considering the spatial distribution of the defects, two statistical representations of the data were used. Exponential probability plots were generated to visually compare defect characteristics distributions. Furthermore, the two sample Kolmogorov-Smirnov (K-S) statistical test explained in the next section was used to statistically determine if any variability between the two distributions observed in the probability plots is significant. The K-S test allows one to compare arbitrary distributions to one another while the distributions do not have to be normal.

Since the sample number of defects gathered from the 3D analysis were large enough in most of the cases, based on the results of the K-S test one can infer if differences that exist between the distributions

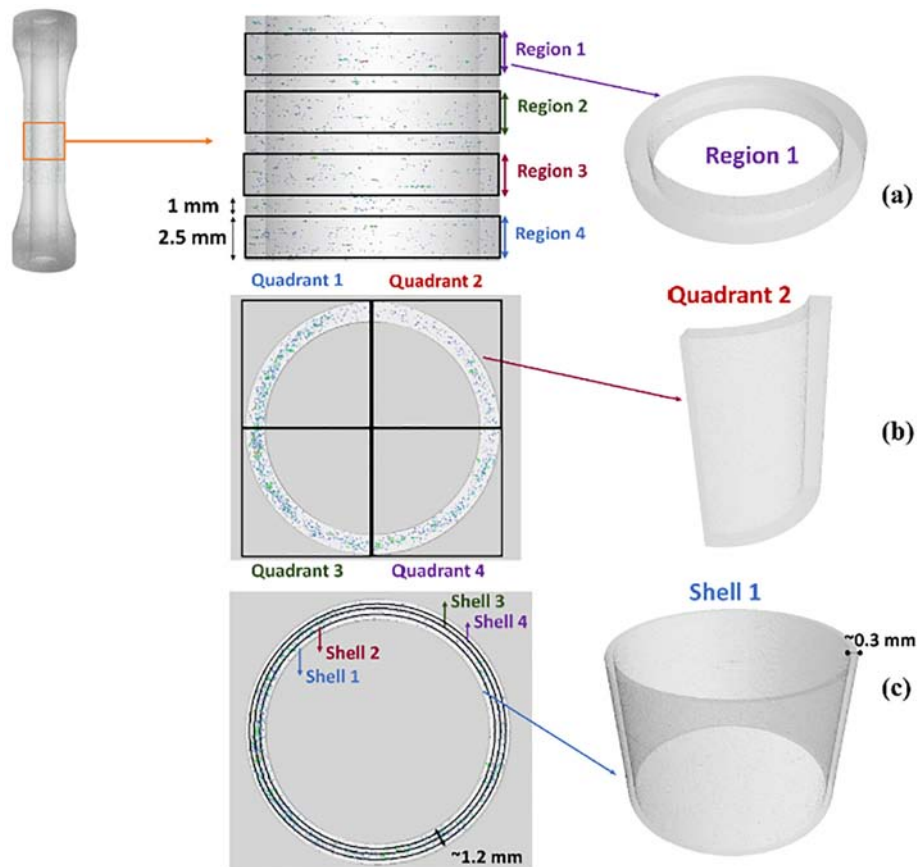


Fig. 4. The micro-CT scanned volume is divided into various sections and variability in distributions of the defect characteristics in these sections are compared, (a) the scanned volume is divided into four equal control volumes sectioned along the build height, (b) the scanned volume is divided into four equal quadrants as control volumes, (c) the scanned volume is divided into four shells with equal thicknesses of ~ 0.3 mm as control volumes.

are significant. Furthermore, the distributions of defect characteristics in duplicate samples were compared in order to study the repeatability between duplicate specimens from the same condition. Distribution of each characteristic in the micro-CT scanned volume from each specimen was compared with the corresponding distribution from the duplicate specimen.

For K-S test to be used on 2D analysis results, data from several cross-sections were necessary to be gathered. For 2D analysis, four cross-sections from the micro-CT scanned volume of the gage section perpendicular to the built direction of an M290 and an AM250 Ti-6Al-4V annealed machined surface specimen, as well as a 17-4 PH M290 annealed as-built surface specimen, were cut and prepared for microscopy. Also, four cross-sections perpendicular to the build direction from the grip section of the same specimens with the thickness of about 6 mm were also cut and analyzed to study the effect of thickness on the viability of defect characteristics. The distributions were compared using the K-S test.

The distribution of the defect characteristics gathered from each polished section was compared with all the other polished sections along the height. Then the data from four random quadrants of each polished section were compared. As the last comparison, the data gathered from rings with equal thicknesses were compared for each cross-section. This procedure was performed to make sure that the distributions were compared in all three dimensions, to study the variability of the data gathered from different cross-sections for each condition, and to observe the trends for the spatial distribution of defects from 2D and comparing them to 3D analysis results.

3.5. Two-sample Kolmogorov-Smirnov (K-S) test

In the one sample K-S test, an empirical distribution function is compared to a theoretical distribution function. The test result is based on the maximum distance between these two curves. The two sample K-S test is a variation of this test. It is generally performed to examine if two data samples come from the same distribution, although it does not identify the distribution. The hypothesis regarding the distributional form will be rejected if the test statistic, D , is greater than the critical value obtained from a table based on the significance level α . This means there is enough evidence that the two sample distributions are different and do not come from the same distribution.

The two sample K-S test compares empirical distribution functions from the two samples, as can be seen in Fig. 5. E_1 and E_2 in this figure are the empirical distribution functions for the two samples and D is the distance between them at each point:

$$D = |E_1(i) - E_2(i)| \quad (2)$$

If the maximum value of D is greater than the critical value, there is enough evidence that the two distributions are different. The convenience of this test is that the distributions do not have to be normal for this comparison. The significance level α equal to 0.01 was used for the comparisons in this study. This results in a test sensitive to a higher difference between distributions.

4. 3D characterization results and discussions

4.1. Analysis of defect characteristics

One important aspect of the 3D analysis is to provide better visualization of various defect characteristics such as diameter, projected area of the defects on various planes, defect volume, and defect morphology which is usually represented by sphericity and aspect ratio. Also, studying the correlation between these characteristics would help for later analysis to represent the defects with their most important attributes which are not necessarily correlated.

A visualization of the sphericity vs. aspect ratio of defects from 3D micro-CT scanning results for Ti-6Al-4V M290 and AM250 annealed specimens is provided in Fig. 6(a). Both defect sphericity and aspect ratio increase moving from a very irregular shape, interconnected, and elongated defect which represents a LOF defect to a spherical pore. Based on the geometrical definitions and nature of the observed defects, defects with sphericities close to 1 and low aspect ratios do not exist. However, there is a possibility for a defect to have the aspect ratios close to 1 and lower sphericity.

A visualization of the circularity vs. aspect ratio of defects from 2D microscopy results is provided in Fig. 6(b). Similarly, both defect circularity and aspect ratio increase moving from a very irregular shape and slender defect which represents a LOF defect to a spherical pore. Again, based on the geometrical definitions and nature of the observed defects, defects with circularities close to 1 and low aspect ratios do not exist. However, there is a possibility for a defect to have the aspect ratios close to 1 and a relatively lower circularity.

For Ti-6Al-4V, M290 machine created slightly higher energy density per unit volume $56.4 \text{ J} \cdot \text{mm}^{-3}$ as opposed to $50 \text{ J} \cdot \text{mm}^{-3}$ for AM250 machine and also had smaller hatch spacing and smaller layer thickness compared to AM250. The better-optimized combination of these parameters resulted in a significantly lower defect content and higher specimen quality for Ti-6Al-4V M290 as opposed to many large and more elongated LOF defects containing un-melted particles observed for AM250.

The average volume fraction of porosity in Ti-6Al-4V M290 vertical annealed machined surface specimens from micro-CT data is 0.002% as opposed to 0.61% for AM250 specimens with the same heat treatment and surface finish conditions. The average volume fraction of porosity in Ti-6Al-4V M290 vertical HIPed machined surface specimens decreased to 0.0004% after HIP. Moreover, 17-4 PH M290 specimens built with an energy density of $72.7 \text{ J} \cdot \text{mm}^{-3}$ showed a different defect structure compared to Ti-6Al-4V M290 specimens with a very high number of small gas porosities ($\sim 50 \mu\text{m}$) and a relatively higher volume fraction of porosity (0.007%).

The defect content of another Ti-6Al-4V specimen built with a different M290 machine using the same process parameters was inspected by optical microscopy to examine the similarity of defect contents. Similar defect structures in terms of the number of defects and the largest defect size was observed for the Ti-6Al-4V M290 annealed as-built surface specimens. In both as-built surface specimens, larger defects ($\sim 150 \mu\text{m}$)

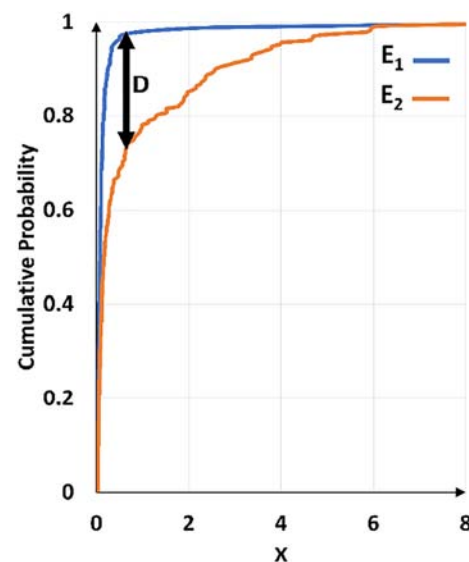


Fig. 5. The 2-sample K-S test compares the values of two empirical distribution functions (E_1 and E_2) from the two distributions at the x where the distance between the curves (D) reaches the maximum value.

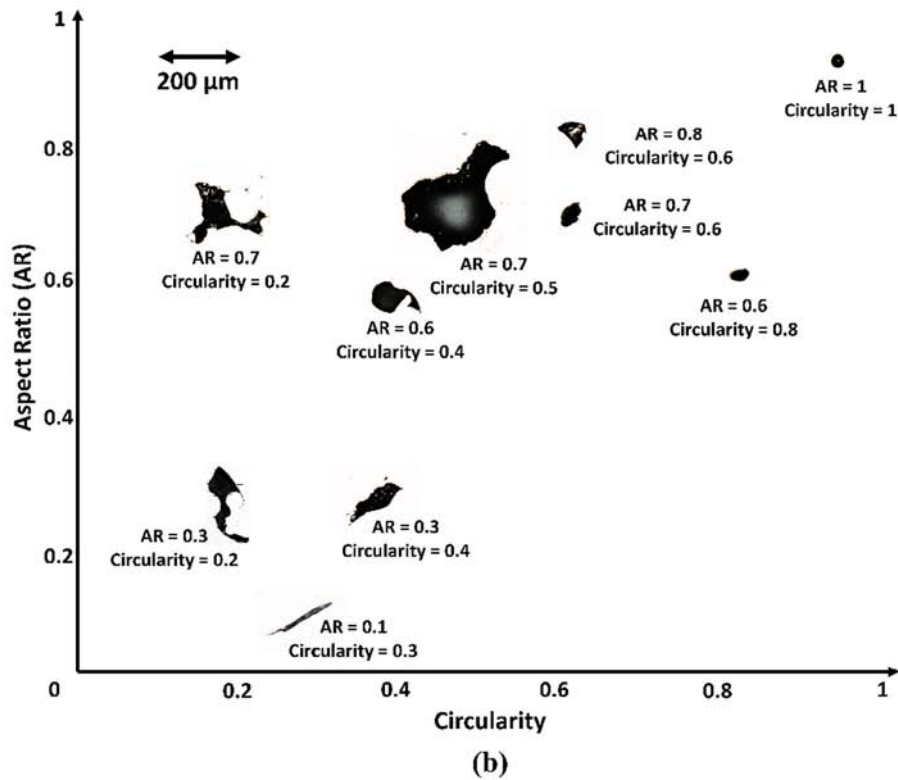
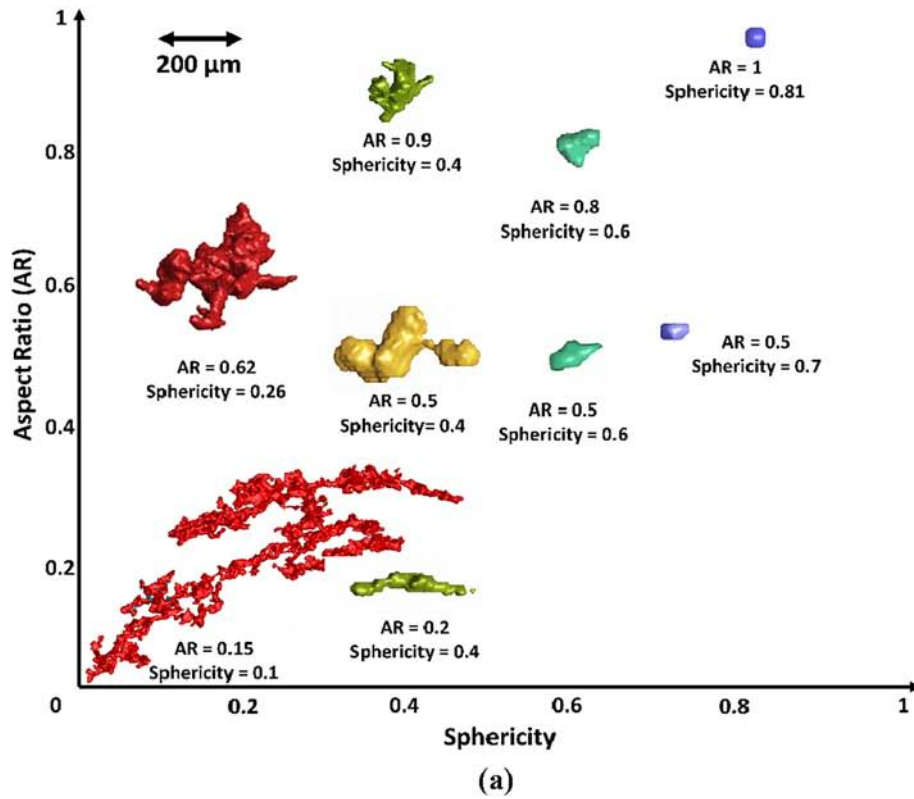


Fig. 6. (a) Aspect ratio (AR) vs sphericity visualization of defects gathered from micro-CT results using software for Ti-6Al-4V AM250 and M290 annealed specimens, (b) Aspect ratio (AR) vs circularity visualization of defects observed during optical microscopy. (Relative size of defects is shown).

were found mostly closer to the inner and outer surfaces, although defects with similar size were occasionally observed further from the surfaces.

A comparison of the projected areas of the vertical Ti-6Al-4V and 17-4 PH specimens defects on three orthogonal planes can be seen in Fig. 7, for two specimens from each condition represented with different

colors. This comparison helps to confirm the plane on which the defects are expanded. The dashed lines are the equal projected areas line for each comparison. Generally, the defects for both groups of Ti-6Al-4V specimens, as can be seen in Fig. 7(a) and (b), are expanded perpendicular to the built direction (on the x-y plane) or parallel to the layers. In contrast, projected areas on the other two planes (x-z and y-z planes) are not significantly different. For both conditions, a random dispersion is found for projected areas on the other planes, as can be seen from a comparison of Fig. 7(a) and (b), which was expected. Defects of AM250 specimens are generally more elongated and show a more pronounced difference between the projected areas parallel and perpendicular to the build direction. This difference is particularly higher for larger defects, representing LOF defects more elongated on the x-y plane with lower aspect ratios.

For 17-4 PH defects, the same comparison is not conclusive, meaning the defects seemed not to be expanded on any particular plane, as can be seen in Fig. 7(d). This is in line with the observations from 2D defect analysis which showed that most of the defects for 17-4 PH are gas porosities closer to a spherical or ellipsoidal shape (Fig. 1(c)). As the number of these gas porosities is high,

some connected gas porosities as presented in Fig. 1(c) were also observed.

Similar comparison for diagonal M290 Ti-6Al-4V specimens, did not show any significant difference between these projected areas. This is consistent with the observations made in this study and in the literature stating that the defects are typically extended parallel to the layers. Therefore, since none of these three projected areas are representing the projected area perpendicular to the build direction their values show similar random patterns. Similarly, for vertical M290 HIPed Ti-6Al-4V specimens the same comparison did not show defects to be expanded in any of these particular directions, as can be seen in Fig. 7(c). The combination of high pressure and temperature during HIP is significantly fusing and shrinking defects and reducing the directionality of the defect structure. This occurs by a significant reduction of the volume and blunting of the edges of LOF defects which result in a more isotropic response in the mechanical behavior as was reported previously [36].

Defect size is usually represented by either diameter, volume, or projected area in the 3D analysis. The correlations between diameter, projected area on the x-y plane (perpendicular to the built direction), and volume of the defects for Ti-6Al-4V M290 and AM250 specimens

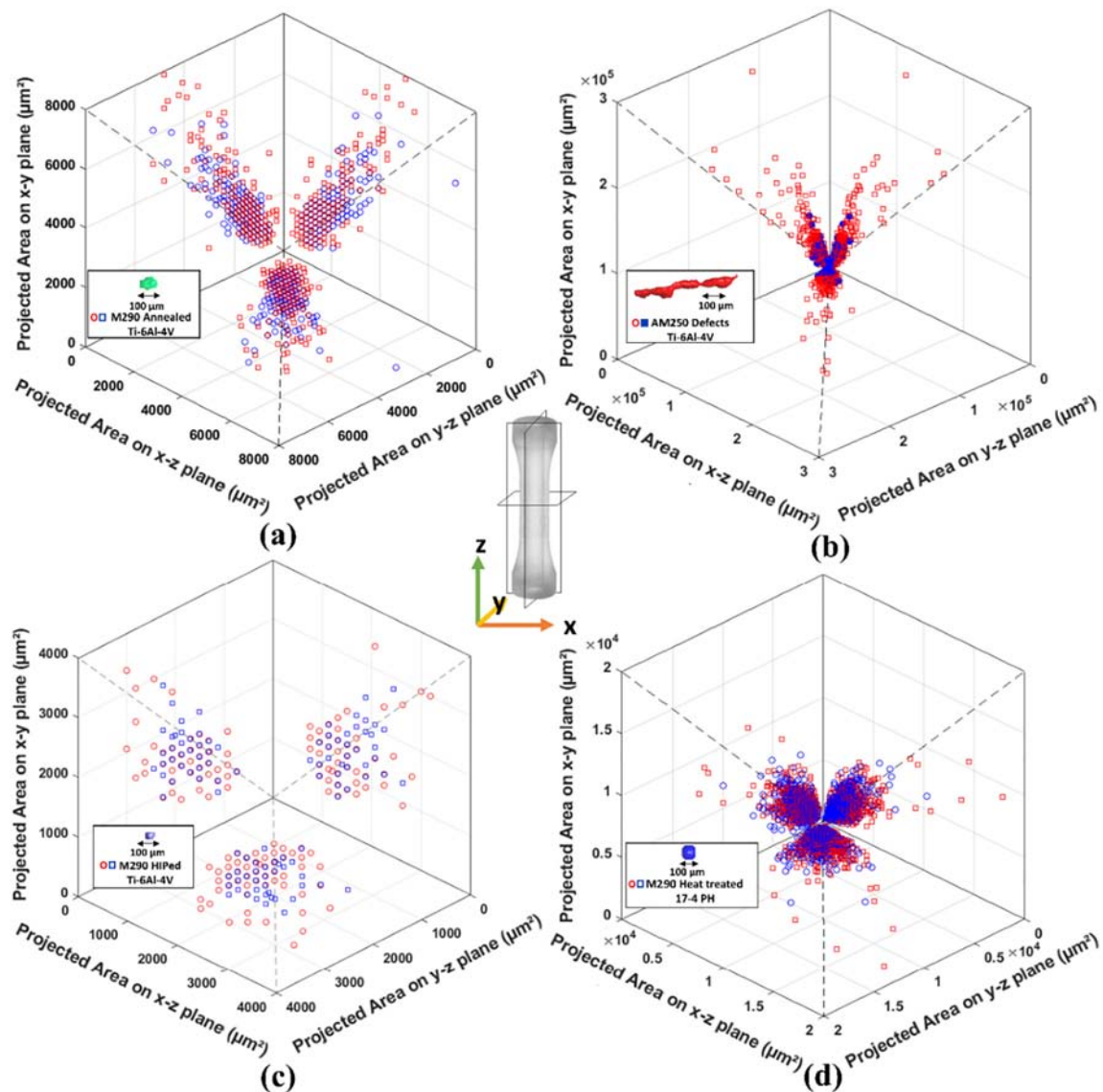


Fig. 7. Comparison of projected areas of the defects for vertical specimens on three planes (projected areas on x-y plane versus projected areas on x-z and y-z planes) gathered from micro-CT scanning for two specimens built for each condition shown with different colors: (a) M290 annealed machined surface Ti-6Al-4V, (b) AM250 annealed machined surface Ti-6Al-4V, (c) M290 HIPed machined surface Ti-6Al-4V, (d) M290 heat treated as-built surface 17-4 PH. (The dashed lines represent the line of equal projected areas for each comparison).

and for 17-4 PH M290 specimens gathered from micro-CT are demonstrated in Fig. 8. The data gathered from two specimens in each case are shown with different colors. The dashed lines represent what the relationship between diameter, projected area, and volume should look like if the defects were perfect spheres. Fig. 8 shows the general trend for each of these two sets of characteristics, and except for the defects with relatively larger diameters, these trends are analogous for duplicate specimens.

The diameter, projected area, and volume of the defects seem to have a better correlation and closer to the dashed line for the Ti-6Al-4V M290 specimens defects, as can be seen in Fig. 8(a) compared to the other two conditions. These defects had shown to be sparse small gas porosities and LOF defects with relatively high sphericities and aspect ratios. A good correlation between these parameters was observed for Ti-6Al-4V M290 HIPed specimens defects as well.

Correlation between these parameters is not as good as one might expect for 17-4 PH M290 specimens defects as can be seen in Fig. 8(c) and data points are not aligned with the dashed lines although these defects are mostly gas porosities. These gas porosities were observed to be ellipsoidal, flattened sphere shape, or bean shape and

randomly oriented rather than a perfect sphere and are not expanded between the layers on the x-y plane as opposed to Ti-6Al-4V M290 specimens defects. Moreover, a fraction of these defects especially closer to the surfaces where defects are closer, is connected porosities (Fig. 1(c)) or very close gas porosities perceived as connected in random directions by the software. The projected area and volume of the defects appear to have a better correlation and closer to the dashed line.

These correlations are far from correlations for perfect sphere and this deviation is more obvious in Fig. 8(b) for Ti-6Al-4V AM250 defects which were mostly larger LOF defects (Fig. 1(a)). Also, many outliers are found that do not follow the general trend of the correlations. The reason that these defects do not have proportionally large projected areas and/or volumes, is the small aspect ratio and/or sphericity of these defects. These defects with large diameters could be slender and narrow and irregularly shaped and, therefore, not necessarily have a large volume and/or projected area. Also, the 3D analysis showed many interconnected defects elongated around the specimen for Ti-6Al-4V AM250. This interconnection could not be perceived from the 2D analysis. This could affect the fatigue crack growth path and create a more critical condition for fatigue performance.

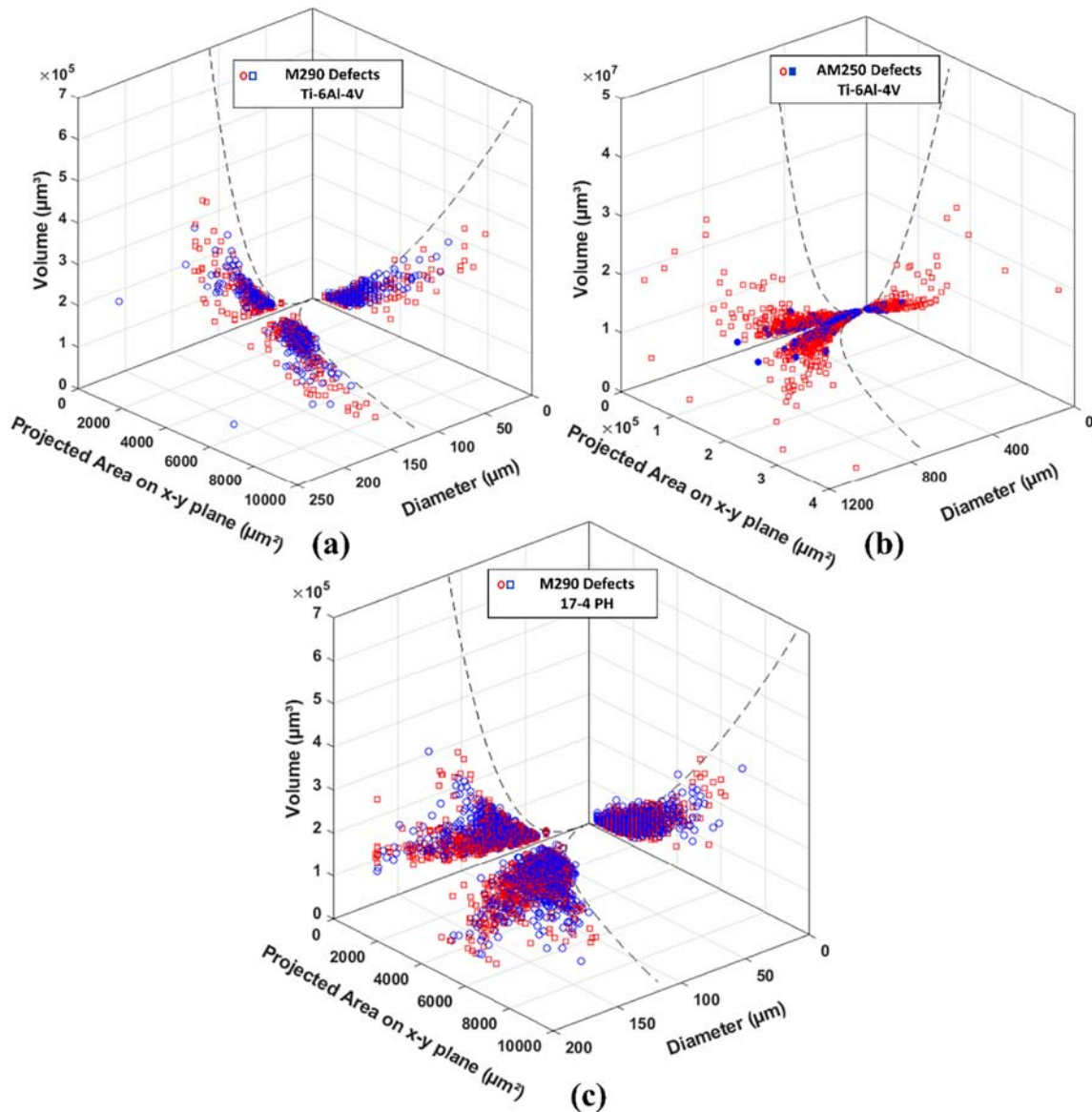


Fig. 8. Correlation of diameter, projected area on the x-y plane, and volume of the defects for vertical specimens gathered from micro-CT scanning for two specimens in each case: (a) Ti-6Al-4V M290 annealed machined surface, (b) Ti-6Al-4V AM250 annealed machined surface, (c) 17-4 PH M290 heat treated as-built surface. (The dashed lines represent the relationship between diameter, projected area, and volume of a perfect sphere).

These critical large diameter defects with irregular shapes and sharp corners along with a high overall volume fraction of porosity could control mechanical properties such as fracture toughness and fatigue lives for these specimens. Based on the above observations to ensure that these defects are represented more accurately in analysis and prediction of mechanical properties, specifically fatigue properties, the size of these defects represented by either diameter, projected area, or volume should be accompanied by the aspect ratio or sphericity of these defects. The correlations between diameter, as a representation of the defect size, with aspect ratio and sphericity of these defects, are shown later. The diameter which generally stands for the longest distance between any two points along the defect selection boundary is used as a representation of overall defect size in the rest of the plots of 2D and 3D analysis results. However, the projected area and volume as representations of defect size are also considered, and discussions are made on which of these parameters is a better indication of the defect size for further analysis.

The repeatability of the process could be tested based on the defect content of the duplicate specimens. This examination was done considering the exponential probability plots, along with a comparison of volume fraction of defects in duplicate specimens, and finally, the K-S test results listed in Table 2. As can be seen in this table, repeatability of defect content for Ti-6Al-4V M290 annealed specimens is not as good as expected, despite the low defect content. It is interesting to see variation between duplicate specimens from one batch, for Ti-6Al-4V specimens built with AM250 machine and M290 machine. This shows that variation can still exist between defect contents of two parts built in one batch with good optimized AM process parameters.

K-S test results listed in Table 2 show that the variation between the duplicate 17-4 PH M290 specimens is noticeably lower compared to Ti-6Al-4V M290 specimens, in spite of the defect density being higher. Better repeatability for 17-4 PH duplicate specimens can be explained by the presence of a high number of gas porosities in these specimens due to the high energy density during the AM process. This made the defect content of duplicate specimens more similar, as opposed to Ti-6Al-4V specimens with a lower number of defects, but containing LOF defects.

Defect sphericity distributions in duplicate specimens are similar for nearly all the conditions, except for Ti-6Al-4V AM250 specimens. This is more significant in the case of as-built surface specimens since large elongated LOF defects close to the surfaces were present, along with smaller LOF defects and some gas porosities throughout the wall thickness. This caused a wider range for variation in values of defects sphericities compared to other conditions.

4.2. Analysis of variability in defect characteristics based on location

K-S test results based on the analysis of 3D characterization data are listed in Table 3. Distributions of diameter, volume, projected area, and

sphericity of the defects based on their location in each specimen were considered. As shown in Fig. 4 for each condition the scanned volume is divided into four control volumes. The distribution of each defect characteristic in each control volume is compared with the other three control volumes. This results in six comparisons in case of each characteristic for each condition per specimen. If equal to or more than half of the comparisons for each condition were showing significant differences, the overall result is highlighted with red color and the percentage of similarity is listed in the table. If more than half of the comparisons are showing no significant difference, the overall result is highlighted with green color with the percentage of similarity listed in the table.

4.2.1. Variability along the build direction

The micro-CT scan results of two specimens for each condition are used for variability analysis. Defect content was analyzed for the middle part of the gage section with uniform thickness considering each defect characteristic of interest. To inspect the variability of the defect characteristics distributions along the build direction as can be seen in Fig. 4 (a), the scanned volume was divided into four equal sub-volumes with 2.5 mm height and a 1 mm gap was considered in between every two sub-volumes. The exponential probability plots for the defect diameter, volume, projected area, and sphericity distributions were depicted to visualize the variability of these defect characteristics distributions along the height of each specimen. The exponential probability plots of defect diameter distributions for the four control volumes along the build direction for different conditions are shown in Fig. 9.

As discussed earlier, only the exponential probability plots for defect diameter are presented here as a representation of defects size although the K-S test results for all these characteristics are later presented in tables. F is the cumulative distribution function value which is used to determine the probability that a random observation taken from a population will be less than or equal to a certain value. These plots show slight differences in defect diameter distributions between four regions of each specimen which are more pronounced for larger defects. Also, probability plots show that the largest defects are randomly placed throughout the analyzed built height for different specimens built with each machine, material, and surface condition and no specific trend is observed in the scanned height for the location of the defect with the largest diameters, projected area, or volume with respect to the build height in the micro-CT scanned volumes. However, it should be noted that the analyzed height is relatively short (15 mm), resulting in a high probability for the laser beam and process parameters stability in this height. This might not be the case for a long part and the variation in process parameters might occur, depending on how well-optimized and stable the process is.

The defect characteristics (diameter, volume, projected area, and sphericity) distributions were compared using the K-S test to examine whether the scatter observed on the probability plots are significant

Table 2

Analysis of repeatability of the defect content for duplicate specimens. The summary of K-S test results based on 3D analysis, on the distribution of characteristics of the defects for duplicate samples for each condition. Two distributions were compared for each case and the value of the K-S test is presented. Green and red colors represent similarity in distributions and difference in distributions, respectively.

Material	AM machine	Build orientation	Post processing	Surface condition	K-S test value			
					Defect characteristics			
					Diameter	Volume	Projected area	Sphericity
Ti-6Al-4V	AM250	V	Annealed	As-built	0.054	0.160	0.134	0.005
Ti-6Al-4V	AM250	V	Annealed	Machined	0.137	0.141	0.169	0.002
Ti-6Al-4V	M290	V	Annealed	Machined	0.242	0.276	0.223	−0.06
Ti-6Al-4V	M290	45°	Annealed	Machined	−0.13	0.004	−0.052	−0.031
Ti-6Al-4V	M290	V	HIPed	Machined	−0.106	−0.106	−0.125	−0.109
17-4 PH	M290	V	Heat Treated	As-built	0.044	0.097	0.085	−0.015

Table 3

The summary of K-S test results based on 3D analysis, on the distribution of characteristics of defects based on their location in the specimen gage section. Six distribution were compared in each case. Green and red colors represent similarity in distributions and difference in distributions, respectively.

Control volume		Material	AM machine	Build orientation	Post processing	Surface condition	Similarity of distributions (%)			
							Defect characteristics			
							Diameter	Volume	Projected area	Sphericity
Along the height	Four equal slices	Ti-6Al-4V	AM250	V	Annealed	As-built	100	83	83	100
		Ti-6Al-4V	AM250	V	Annealed	Machined	100	100	83	100
		Ti-6Al-4V	M290	V	Annealed	Machined	100	100	100	100
		Ti-6Al-4V	M290	45°	Annealed	Machined	100	100	100	100
		Ti-6Al-4V	M290	V	HIPed	Machined	100	100	100	100
		17-4 PH	M290	V	Heat Treated	As-built	83	100	100	100
Around the specimen axis	Four equal quadrants	Ti-6Al-4V	AM250	V	Annealed	As-built	0	0	17	17
		Ti-6Al-4V	AM250	V	Annealed	Machined	33	33	33	65
		Ti-6Al-4V	M290	V	Annealed	Machined	100	100	100	100
		Ti-6Al-4V	M290	45°	Annealed	Machined	100	100	100	100
		Ti-6Al-4V	M290	V	HIPed	Machined	100	100	100	100
		17-4 PH	M290	V	Heat Treated	As-built	65	100	100	100
Through thickness	Four shells with equal thickness	Ti-6Al-4V	AM250	V	Annealed	As-built	0	0	0	0
		Ti-6Al-4V	AM250	V	Annealed	Machined	83	83	100	100
		Ti-6Al-4V	M290	V	Annealed	Machined	100	100	100	100
		Ti-6Al-4V	M290	45°	Annealed	Machined	100	100	100	100
		Ti-6Al-4V	M290	V	HIPed	Machined	100	100	100	100
		17-4 PH	M290	V	Heat Treated	As-built	33	17	33	17

and there is sufficient evidence to conclude that the underlying distributions of the defect diameters in different sections of the built height are different. The distribution of the defect characteristics in each section was compared with the other three sections along the height as explained earlier. The K-S test results as listed in Table 3, do not show any significant difference between the defect characteristics distributions gathered along the built height for any of the materials, machines, or surface conditions for the micro-CT scanned volume. This means that considering each of these sections would provide an acceptable representation of the defect distribution in the whole scanned volume of the gage section. These data can also be combined to a single population and this was done for the subsequent 3D analysis to study variability around the specimen axis and through the specimen thickness.

4.2.2. Variability around the specimen axis

To inspect the variability of the defect characteristics distributions around the specimen's axis of symmetry, as can be seen in Fig. 4(b), the scanned volume was randomly divided into four equal quadrants parallel to specimen axis with equal heights of 10 mm each. Exponential probability plots of defect diameter distributions for the four quadrants as control volumes can be seen in Fig. 10. Probability plots show distinct differences for the distribution of defect diameters in different quadrants around AM250 specimens for both as-built and machined surface conditions, with one or two quadrants containing a more defects with larger defect sizes.

Generally, the number of specimens in one batch and the location of each on the base plate could affect the inter-layer time interval for the specimens to cool down between deposited layers and would affect the final defect structure. The observations made here could indicate that the build pattern and scanning contour which might cause variations in scan speed, as well as the location of the specimen on the platform, and the proximity of a specimen to the rest of the specimens on the build platform could influence the distribution of the defects, especially if the process is not well-optimized. Critical defects could be accumulated on a particular side and not randomly distributed, even around a specimen with a symmetrical geometry.

This variability is not that significant in M290 vertical specimens both for Ti-6Al-4V and 17-4 PH. M290 diagonal specimens also did

not show any significant variability in distribution of defect characteristics around the specimen axis although the diagonal specimens are not made symmetrically around the specimen axis and the roughness of the diagonal specimens had been shown to be higher on the downward-facing surfaces (down-skin) as compared to the upward-facing surfaces (up-skin) [36]. These observations show that by better optimizing the process parameters and choosing the right build pattern, the variability between the defect characteristics distributions around the specimen is highly reduced and a more uniform and a more random dispersion of defects can be achieved.

Comparisons of the defect characteristics distributions for four quadrants as control volumes using the K-S two sample test confirm these observations as can be seen in Table 3. There is a significant difference between defect diameter distributions gathered from various quadrants of the scanned volume for AM250 specimens for both as-built and machined surface conditions. This means that characterization of only one of these control volumes will not provide a comprehensive picture of the distribution of defects in the specimens and might cause missing critical information. K-S tests show no significant variability in quadrants for M290 annealed specimens and as expected no significant difference between the distributions after HIPing.

4.2.3. Variability throughout the wall thickness

To inspect the variability of the defect characteristics distributions through the wall thickness of the specimens, as shown in Fig. 4(c), the scanned volume was divided into four shells with thicknesses of ~0.3 mm and heights of 10 mm. Exponential probability plots for the defect distribution in these four shells are shown in Fig. 11. These plots show very distinct differences between the distributions of defect diameter in different shells for as-built surface specimens. These results were confirmed by the K-S test results from 3D analysis as listed in Table 3. The K-S test results in this table do not show significant differences between the shells of machined surface specimens and the distribution of defects through wall thickness is more uniform after removing the surface defects by machining.

The larger defects seem to be located closer to inner and/or outer surfaces. This shows the proximity to the surface could influence defect size and density. This can be detrimental particularly for fatigue

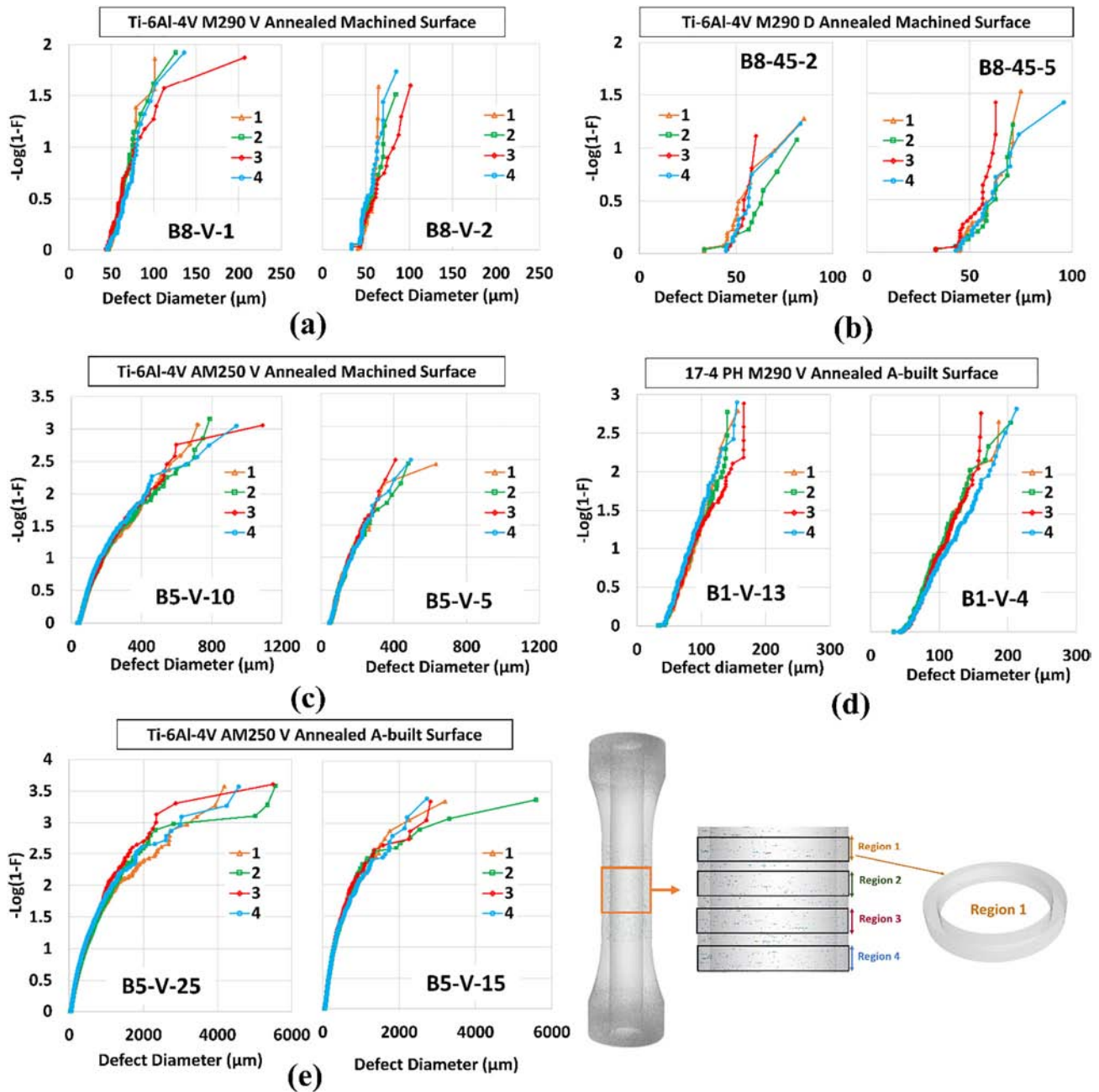


Fig. 9. Comparisons of defect diameter distributions for four equal control volumes from different build heights using exponential probability plots, (a) Ti-6Al-4V M290 vertical annealed machined surface, (b) Ti-6Al-4V M290 vertical HIPed machined surface, (c) Ti-6Al-4V AM250 vertical annealed machined surface, (d) 17-4 PH M290 vertical heat treated as-built surface, (e) Ti-6Al-4V AM250 vertical annealed as-built surface.

performance since the surface defects usually experience higher stresses especially in loadings involving shear or bending where a stress gradient is present. Even in uniaxial fatigue, the defects closer to the surface create higher stress concentrations compared to internal defects and therefore, are more critical [37].

Volume fractions of defects in four shells for different conditions are compared in Fig. 12 and a visualization of the 3D model for each case is provided. Higher porosity observed for outer and inner surface shells in as-built surface specimens could be caused during the initial and final contour scanning of each layer, which might be conducted at a different scan speed than the steady speed adopted in the rest of the cross-section.

The melt pool size and consequently the distribution of the defects in the regions closer to the surface might be affected by both the control software altering the beam parameters and the lower conductivity of

the surrounding powder in comparison to the solid material [37]. In a study by Seifi et al. [11] the greatest intensity of defects was observed clustered parallel to the outside walls of their cuboid specimens. Change in the spatial distribution of defects was associated with the beam travel direction and the potential role of the hatching pattern used during processing was highlighted. It was explained that different locations of the build undergo different thermal cycles based on different directions and speeds of beam travel.

Fig. 12(a), (b), and (c) shows Ti-6Al-4V M290 vertical machined surface specimens in annealed and HIPed conditions and diagonal machined surface specimens in the annealed condition, respectively. The outer shells in all these machined surface specimens show a relatively lower volume fraction of porosity. The variation between the volume fraction of defects in Ti-6Al-4V M290 vertical HIPed duplicates is considerably lower compared to the annealed condition. The combination of

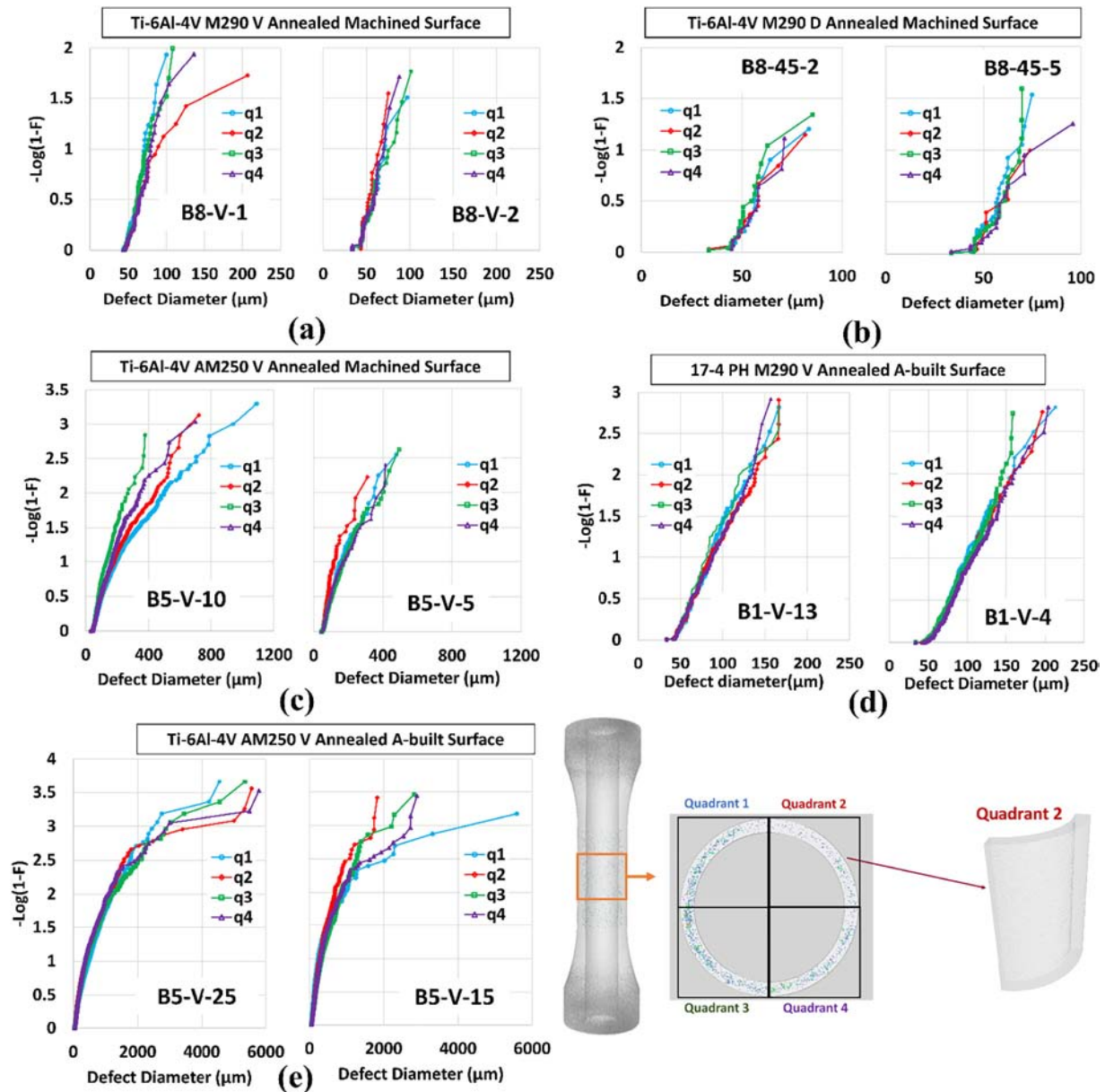


Fig. 10. Comparisons of defect diameter distributions for four equal quadrants as control volumes using exponential probability plots, (a) Ti-6Al-4V M290 vertical annealed machined surface, (b) Ti-6Al-4V M290 vertical HIPed machined surface, (c) Ti-6Al-4V AM250 vertical annealed machined surface, (d) 17-4 PH M290 vertical heat treated as-built surface, (e) Ti-6Al-4V AM250 vertical annealed as-built surface.

high pressure and temperature during HIP is significantly reducing and fusing the defects and result in a more similar final defect content between different specimens. Interestingly, variation between the volume fraction of defects in Ti-6Al-4V M290 diagonal annealed duplicates is lower compared to vertical ones as seen in Fig. 12(c), which might be associated with the different build patterns.

The 3D K-S test results in Table 3 show variability through thickness for 17-4 PH as-built surface specimens manufactured with M290 machine. A primary reason is that although almost all the defects observed for 17-4 PH specimens are small gas porosities, the porosities near inner and outer surfaces are closer together (Fig. 1(c)), which caused the interpretation of these small adjacent defects as large elongated defects by the software. As shown in Fig. 12(d), the highest volume fraction of defects in these specimens are observed for inner surface shells.

As seen in Fig. 12(a) and (e), the Ti-6Al-4V M290 annealed machined surface specimens contain a significantly lower volume fraction

of porosity and a lower difference between their various shells is observed, compared to AM250 specimens due to the better-optimized process parameters. The Ti-6Al-4V AM250 specimens shown in Fig. 12(e) and (f) have similar final thicknesses. As-built surface specimens shown in Fig. 12(f) were built to final thickness and specimens shown in Fig. 12(e) were manufactured with a slightly larger thickness and machined from both inner and outer surfaces to the final thickness. Fig. 12(f) shows that for as-built specimens a significant increase is observed in the volume fraction of defects moving from the middle shell to the surface shells. This phenomenon was consistently observed in all the studied as-built surface specimens. After machining the surface to an appropriate depth, a large portion of these defects was removed. Therefore, as shown in Fig. 12(e), the volume fraction of defects in surface shells of machined surface specimens is significantly lower and closer to the values for the inner shells of the as-built surface specimens presented in Fig. 12(f).

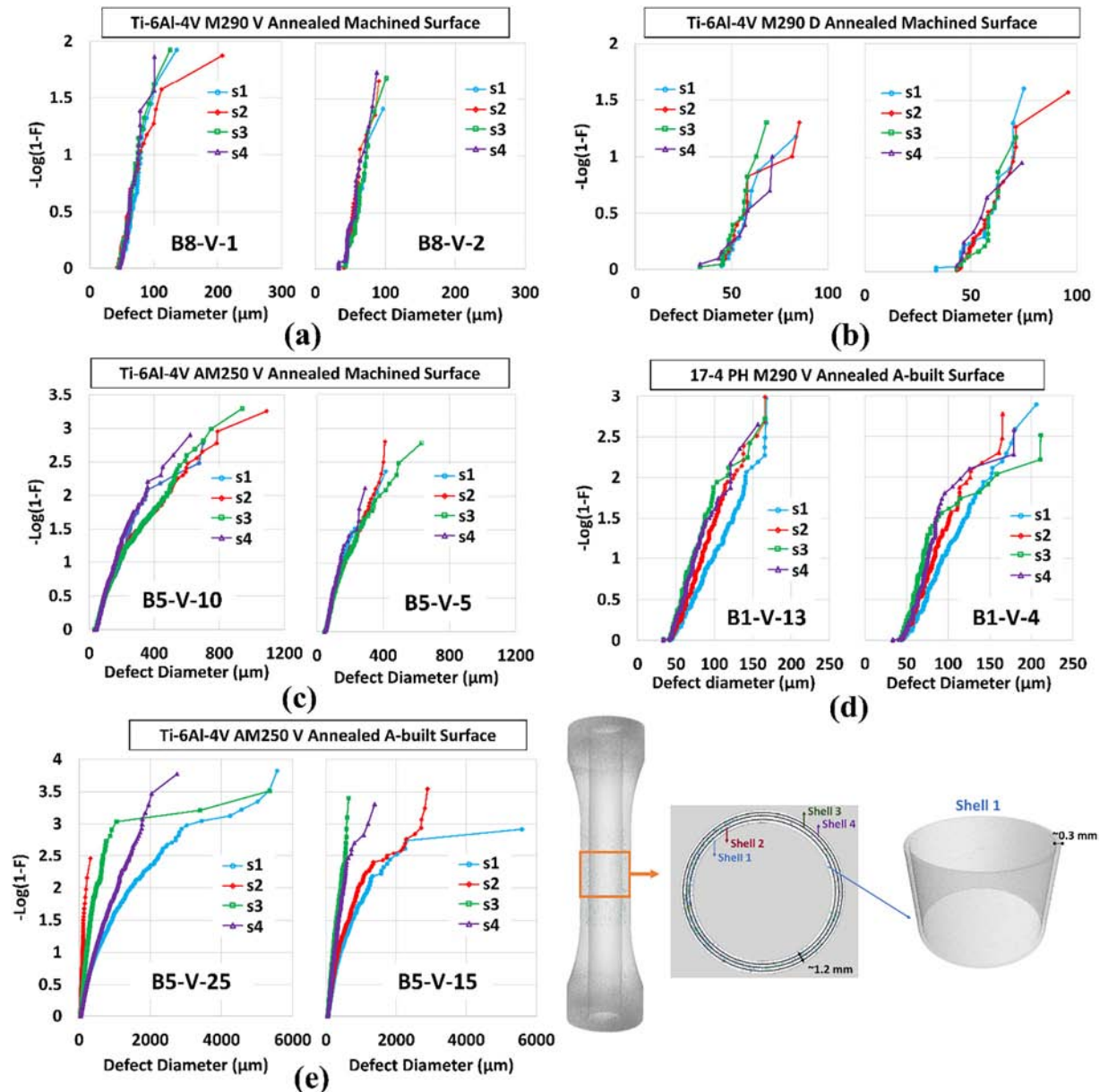


Fig. 11. Comparisons of defect diameter distributions for four shells with equal thickness as control volumes using exponential probability plots, (a) Ti-6Al-4V M290 vertical annealed machined surface, (b) Ti-6Al-4V M290 vertical HIPed machined surface, (c) Ti-6Al-4V AM250 vertical annealed machined surface, (d) 17-4 PH M290 vertical heat treated as-built surface, (e) Ti-6Al-4V AM250 vertical annealed as-built surface.

5. 3D versus 2D defect characterization

3D defect characterization results of the tubular specimens were compared to conventional 2D metallographic optical microscopy measurements for the same specimens. The goal was to investigate if similar information could be collected from both methods and to assess the advantages of each method for specimens with various defect contents. A slice from the micro-CT scanned model perpendicular to the build direction is shown in Fig. 13(a) along with the 2D image taken from the same section with optical metallography as shown in Fig. 13(b) for a Ti-6Al-4V AM250 annealed as-built surface specimen. Having a fair resolution with a voxel size of about 14 μm for micro-CT scanning and staying away from this threshold, the smallest defect diameter gathered from micro-CT data was about 35 μm . The optical microscopy, on the other hand, provided high-resolution images with the smallest defect diameter equal to 5 μm .

The optical microscopy image in Fig. 13(b) provides a clearer picture of the details such as partially-melted particles and the irregular shape

and sharp corners of the LOF defects. The higher concentration of the defects near inner and outer surfaces of the as-built specimens as was discussed earlier, is clearly visible in Fig. 13(a) and (b). Also, it is observed from both images that the defects on the right side of this cross-section are larger and more elongated. These observations agree with the results of the K-S test on 3D data showing significant variability in defect distributions through wall thickness and around the specimen axis for Ti-6Al-4V AM250 annealed as-built surface specimens.

Three micro-CT scanned specimens with different conditions were cut for optical metallography. Four cross-sections from the thinner gage section and four cross-sections from the thicker grip section of each specimen were cut and characterized. K-S test results on 2D data, analyzing distributions of feret diameter, area, and circularity of the defects based on their location in each specimen are listed in Table 4. For both thinner gage section and thicker grip section, distribution of each defect characteristic on each polished section was compared with the other three polished surfaces from the same specimen. This resulted in six comparisons for each characteristic per specimen. Similar to the

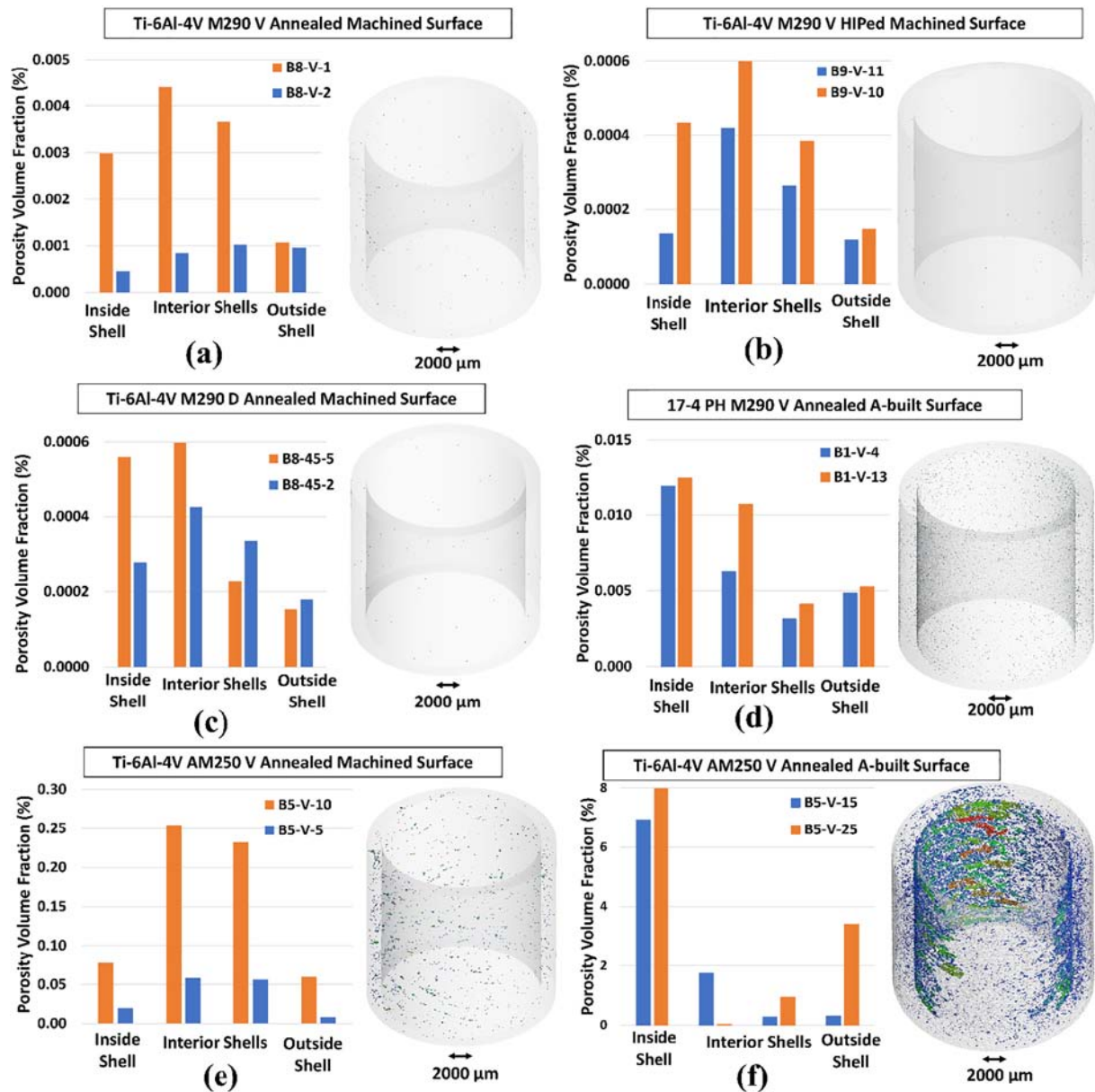


Fig. 12. Comparisons of internal defect volume fraction percentage for four shells with equal thickness as control volumes, (a) Ti-6Al-4V M290 vertical annealed machined surface, (b) Ti-6Al-4V M290 vertical HIPed machined surface, (c) Ti-6Al-4V M290 diagonal annealed machined surface, (d) 17-4 PH M290 vertical heat treated as-built surface, (e) Ti-6Al-4V AM250 vertical annealed machined surface, (f) Ti-6Al-4V AM250 vertical annealed as-built surface. (The rough surface was removed by the software before defect analysis).

3D analysis, as explained in Section 5, the overall result is highlighted with green or red color in Table 4 and the percentage of similarity is listed in the table. Data for each defect characteristic from corresponding quadrants and corresponding rings on the polished surfaces were combined and compared with the three other resulting distributions using the K-S test as explained.

Although from 3D analysis variabilities in defect distributions along the build height of the micro-CT scanned volumes were not significant, the 2D results show different defect distributions on four cross-sections along the height. This is more significant for AM250 specimens due to the presence of large LOF defects. Based on which portion of these large irregular shape defects were cut through, the resulting defect distribution on the polished surface is different. For M290 specimens containing a low number of smaller defects with higher sphericities, the results gathered from different polished surfaces are more similar. Also, there is a more noticeable difference between the defect distributions on polished surfaces for 17-4 PH M290 specimens compared to the

Ti-6Al-4V M290 specimens which could be due to the very high number of gas porosities found in these specimens.

The variability between defect distributions from four polished surfaces cut from the thicker grip section of AM250 specimen is less significant compared to its thinner gage section based on K-S test results listed in Table 4. This could be due to the high density of large LOF defects which provided a higher probability of cutting through defects. As is explained later, the surface fraction of the defects for the thicker sections of Ti-6Al-4V AM250 specimens was significantly higher than thinner ones. Data from a higher number of cross-sections should be gathered and combined for 2D analysis results to be reliable and more representative of the actual defect population, particularly for specimens with a low number of large LOF defects.

Similar to the trends observed in 3D analysis, the 2D analysis showed significant differences between defect characteristics distributions on different quadrants of AM250 specimen polished surfaces, with one or two quadrants containing a higher population of larger

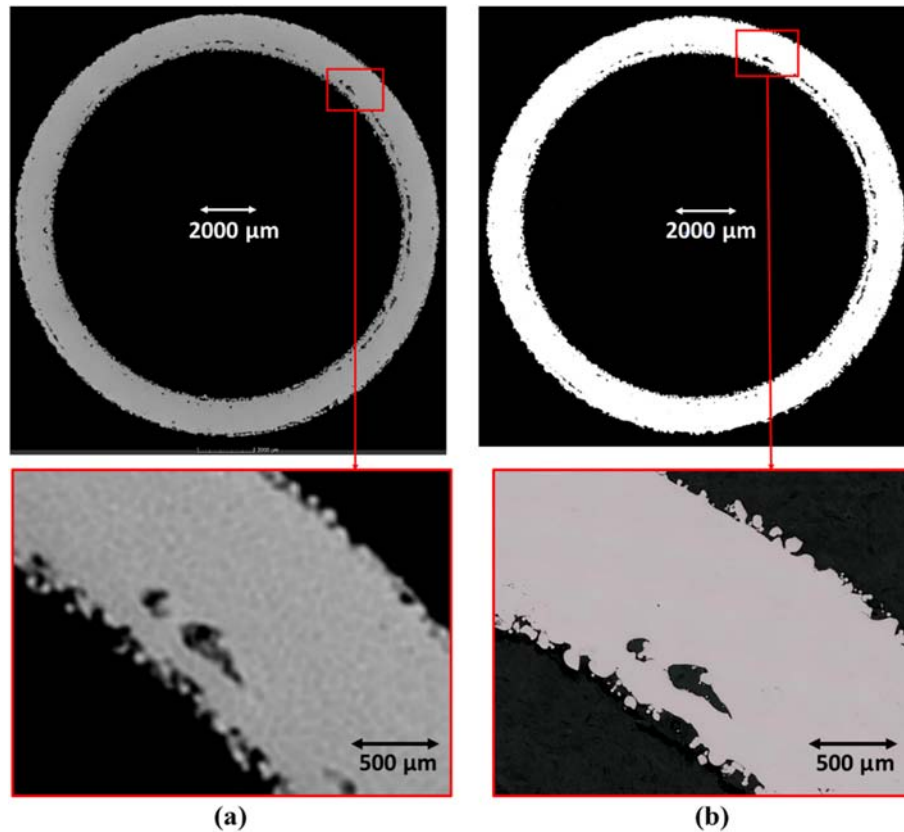


Fig. 13. (a) Horizontal section of the 3D reconstructed model of a Ti-6Al-4V AM250 vertical annealed as-built surface specimen from micro-CT scanning with a 14 μm voxel size, (b) optical microscopy image of the same section after cutting and polishing.

defects. Also, no significant difference between quadrants is observed for well-optimized M290 specimens. Similar to 3D analysis results, K-S test results for 2D data do not show significant differences between defect characteristics distributions gathered from different rings for the machined surface specimens, except for the thicker grip section of

AM2590 Ti-6Al-4V specimens. However, more variability is observed between the rings for 17-4 PH M290 specimen with the as-built surface as shown in Table 4.

The volume fraction of defects in the micro-CT scanned part of the gage sections and the average surface fraction of defects gathered

Table 4

The summary of K-S test results based on 2D analysis, on the distribution of characteristics of the defects based on their location in the specimen. Six distribution were compared in each case. Green and red colors represent similarity in distributions and difference in distributions, respectively.

Control surface		Material	AM machine	Build orientation	Post processing	Surface condition	Thickness (mm)	Similarity of distributions (%)		
								Defect characteristics		
								Feret diameter	Area	Circularity
Along the height	Four cross-sections	Ti-6Al-4V	AM250	V	Annealed	Machined	~1.2	17	17	33
		Ti-6Al-4V	AM250	V	Annealed	Machined	~6	67	67	67
		Ti-6Al-4V	M290	V	Annealed	Machined	~1.2	100	100	100
		Ti-6Al-4V	M290	V	Annealed	Machined	~6	100	100	100
		17-4 PH	M290	V	Heat Treated	As-built	~1.6	50	50	67
		17-4 PH	M290	V	Heat Treated	As-built	~6	50	67	67
Around the specimen axis	Four equal quadrants	Ti-6Al-4V	AM250	V	Annealed	Machined	~1.2	33	17	83
		Ti-6Al-4V	AM250	V	Annealed	Machined	~6	33	33	67
		Ti-6Al-4V	M290	V	Annealed	Machined	~1.2	100	100	100
		Ti-6Al-4V	M290	V	Annealed	Machined	~6	100	100	100
		17-4 PH	M290	V	Heat Treated	As-built	~1.6	100	100	100
		17-4 PH	M290	V	Heat Treated	As-built	~6	100	100	100
Through thickness	Four rings with equal thickness	Ti-6Al-4V	AM250	V	Annealed	Machined	~1.2	100	100	100
		Ti-6Al-4V	AM250	V	Annealed	Machined	~6	67	67	100
		Ti-6Al-4V	M290	V	Annealed	Machined	~1.2	100	100	100
		Ti-6Al-4V	M290	V	Annealed	Machined	~6	100	100	100
		17-4 PH	M290	V	Heat Treated	As-built	~1.6	100	100	100
		17-4 PH	M290	V	Heat Treated	As-built	~6	67	67	100

from four polished surfaces cut from the same volume are compared in Fig. 14(a). The first two columns represent the surface fractions of defects larger than 5 μm and 35 μm , respectively, from 2D defect analysis of a 17-4 PH M290 heat treated specimen. Error bars indicate the actual variation between the surface fraction of defects for four polished sections. The 35 μm threshold was chosen for a better comparison of the 2D surface fraction with the 3D volume fraction results. The volume fraction of defects lies within the error band of the measurements for surface fraction of defects with 35 μm threshold. A high number of small round/spherical defects exist in these specimens. Therefore, the surface fraction of defects from the 2D analysis is close to the volume fraction of defects from 3D analysis using a similar threshold of 35 μm . However, the surface fraction result with a 5 μm threshold is significantly higher in this case. This is due to the presence of a high number of very small gas porosities in 17-4 PH M290 heat treated specimens.

The next two columns represent the surface fractions of defects for a Ti-6Al-4V M290 annealed specimen. The volume fraction, in this case, is closer to the surface fraction with the same defect threshold of 35 μm but the difference between these two values is noticeable. A higher number of cross-sections should be analyzed to achieve surface fraction results comparable to the actual volume fraction of defects due to the low density of defects. The surface fraction with a 5 μm threshold is higher due to the existence of defects between 5 and 35 μm .

The next two columns represent the surface fractions of defects gathered from the 2D analysis of a Ti-6Al-4V AM250 annealed

machined surface specimen. The volume fraction here is higher than the surface fraction results even with a 5 μm threshold for the defect size. The primary explanation is that for Ti-6Al-4V AM250 annealed specimens, very large LOF defects are dominant. Based on which portions of these defects were cut through for 2D analysis, the surface fraction results for different polished surfaces are very different even with a 35 μm threshold. This can result in a considerable difference between the measured surface fraction of defects and the volume fraction of defects unless a high number of polished sections are observed. Cutting and polishing several cross-sections consecutively very close together could provide a more realistic perspective of the defect content.

The density of the defects in the thicker grip section showed to be slightly higher compared to thinner gage section for 17-4 M290 specimen containing a high number of mostly round gas porosities and showed to be significantly higher for Ti-6Al-4V AM250 specimen containing a high number of large LOF defects as observed in Fig. 14(b). However, the density of defects for Ti-6Al-4V M290 containing a low number of both LOF defects and gas porosities does not show any difference between sections with different thicknesses.

2D and 3D methods reveal the same trends in terms of the spatial distribution of the defects throughout the specimens and how it changes with optimization of the process parameters and with post-processing. However, the 2D method requires characterization of several cross-sections to achieve a realistic representation of the defect content. 2D defect characterization can provide high resolution in

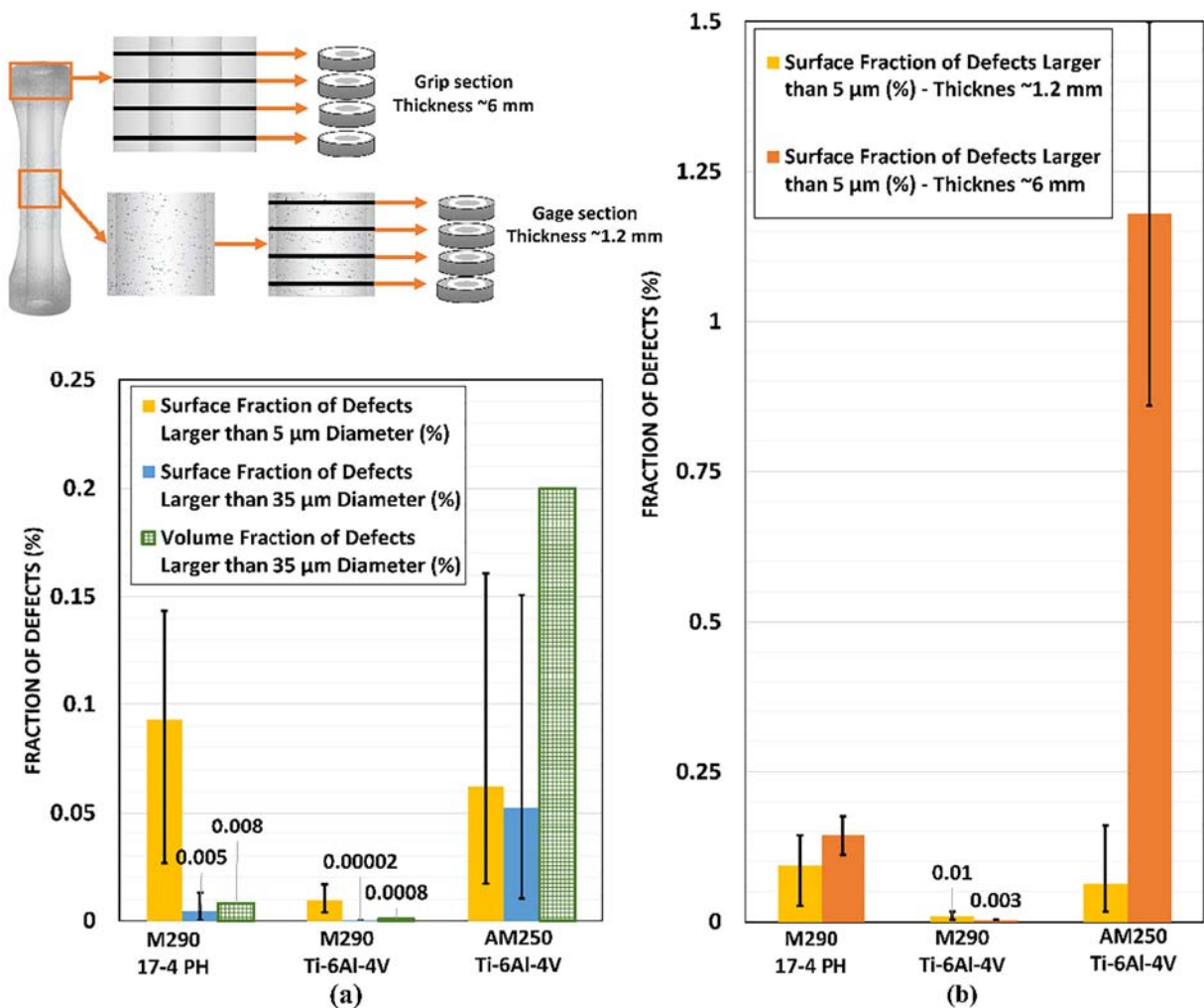


Fig. 14. (a) Comparison of defect volume fraction percentage of the micro-CT scanned volume of gage section with average defect surface fraction of four polished sections cut from same the scanned volume (error bars indicate the variation between the four polished section results), (b) comparison of average surface fraction percentage of defects from the grip section (thickness ~6 mm) with surface fraction percentage of defects from the gage section (thickness ~1.2–1.5 mm).

cases that high-resolution micro-CT scan results are not available and reliable results if the appropriate number of cross-sections are analyzed based on the defect content.

Correlation of aspect ratio, circularity/sphericity, and diameter of the defects gathered from 2D and 3D analysis are shown in Fig. 15. Defects larger than 35 μm diameter for 3D analysis and defects larger than 5 μm diameter for 2D analysis are shown. Largest defects detected in 2D and 3D analysis show both low circularity/sphericity and aspect ratio. These defects create higher stress concentrations which makes them more critical for fatigue performance. The size and complex morphology and interconnected nature of very large defects, such as for Ti-6Al-4V AM250 specimens, might not be perceived correctly by 2D analysis. Although by moving towards better-optimized process parameters and for specimens containing smaller defects, 2D analysis results become more reliable.

Almost all the defects smaller than 35 μm which are observed in 2D analysis, have sphericity equal or larger than 0.7 which in general corresponds to gas porosities. No gas porosity (sphericity larger than 0.7) larger than 100 μm in diameter is observed for any of the materials

and manufacturing machines. These small defects are not observed in the 3D analysis because to stay away from resolution limits (14 μm) each detected defect contained at least 8 voxels in volume.

Although based on the observations from 2D images, almost all the defects observed for 17-4 PH are porosities smaller than 80 μm , 3D results in Fig. 15(a) show defects as large as 200 μm in diameter with low aspect ratios for 17-4 PH. Based on comparisons of 2D and 3D results, these defects are gas porosities very close together which were perceived as connected and are shown as long slender defects by the software during 3D analysis. This was due to the factors such as the limitation in resolution, noise, image artifacts, and algorithm used for defect analysis. In application, the interaction between these defects could happen and they might connect rapidly during the formation of a crack.

Comparing 2D results in Fig. 15(a), (b), and (c) with the corresponding 3D results in Fig. 15(d), (e), and (f), for all conditions the largest defect diameter detected in 2D analysis is smaller than the one detected in 3D analysis. The reason could be either the complicated 3D shape of LOF defects or the fact that it is statistically more likely to cut round pores

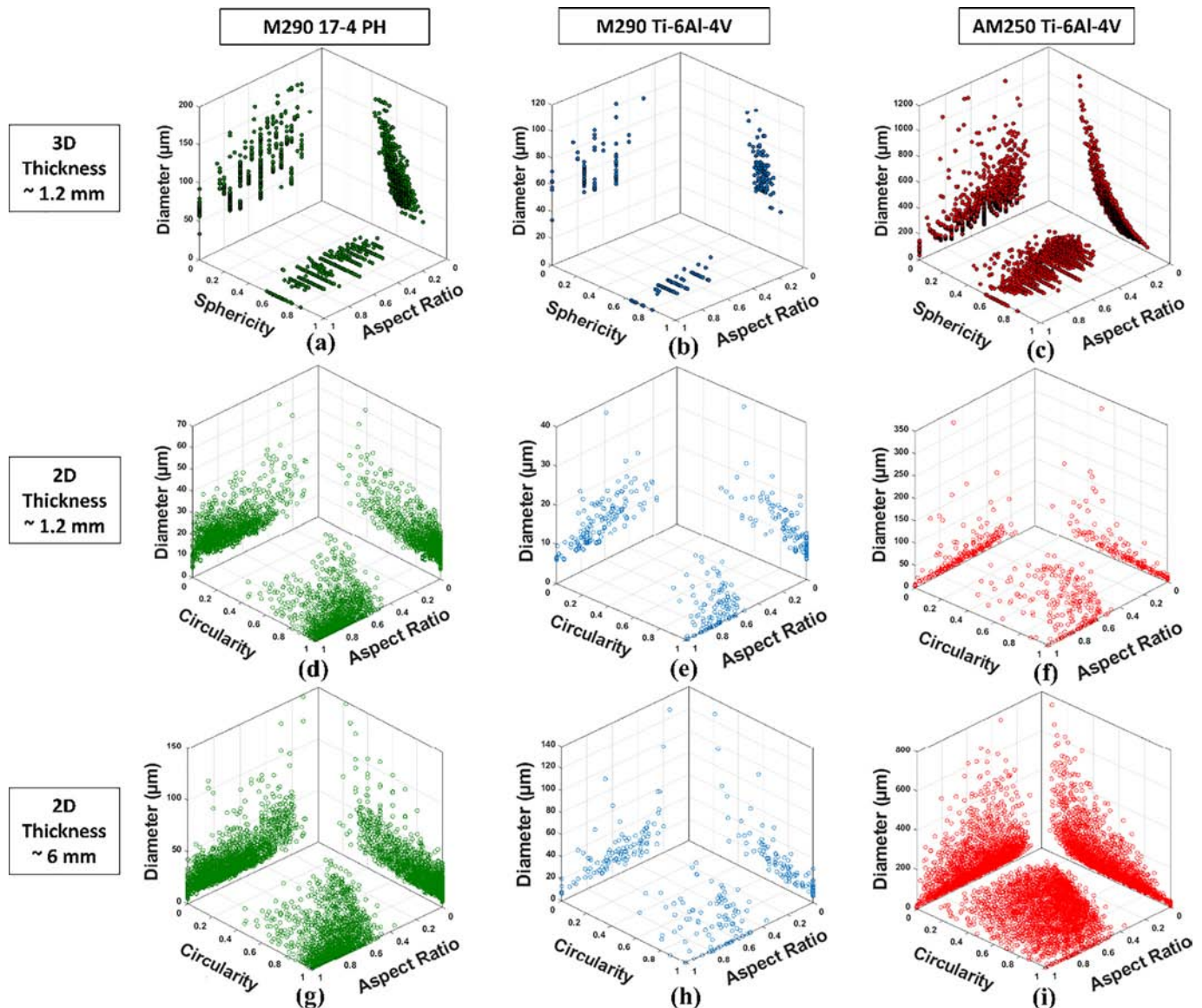


Fig. 15. 3D defect analysis results from micro-CT (~14 μm voxel size) of a 10 mm length of gage sections of tubular L-PBF specimens (a–c); 2D defect analysis results from four polished surfaces of the same micro-CT scanned gage sections with thicknesses ~1.2–1.5 mm (d–f); 2D defect analysis results from four polished surfaces of grip sections of the same specimens with thickness ~6 mm (g–i). (a), (d), and (g) M290 17-4 PH heat treated as-built surface specimen; (b), (e), and (h) M290 Ti-6Al-4V annealed machined surface specimen; (c), (f), and (i) AM250 Ti-6Al-4V annealed machined surface specimen.

not across the middle but through their side [30]. The difference between the perceived overall size of the largest defects from 2D and 3D analysis is considerably higher for Ti-6Al-4V AM250 annealed specimens due to the presence of large irregularly shaped interconnected LOF defects.

Based on 2D results for grip sections seen in Fig. 15(g), (h), and (i), the size of the largest defects in thicker grip sections is larger for all three conditions compared to the thinner gage sections. It has been mentioned in previous studies for SLM of Al-Si10-Mg [38] and 316 L [39] that the region of reduced pore size may be associated with a decreased cooling rate. Applying the same explanation, the thicker grip section contains more consolidated material compared to the thinner gage section. The thinner section is surrounded with more feedstock powder with interstitial air-filled voids and small contact areas between particles which is more insulating than the consolidated material and may result in a lower cooling rate. Conversely, other studies on other manufacturing methods had associated the lower cooling rate with larger defects [38].

Characterization and control of process-related defects and anomalies and their impact on part durability are among the main areas of concern that must be thoroughly addressed for qualification and certification of safety-critical AM parts. As a result of the random nature of these defects and the lack of ability to fully predict, prevent, and eliminate them, failure due to the presence of these defects such as gas porosities and LOF defects needs to be considered and assessed. Moreover, variability in defect characteristics which was the focus of this study caused by the variability in component geometry, AM machine process parameters, and/or beam source/material interactions, and lack of repeatability between two parts manufactured with the same condition could result in variability in the mechanical performance.

6. Summary and conclusions

Variability of the defect characteristics and their distributions within an AM part was examined in this study. The correlation between the defect characteristics was assessed and characterization results gathered from 2D (digital microscopy) and 3D (CT) defect characterization methods were discussed and compared. Distributions of defect characteristics based on their location throughout the L-PBF specimens were analyzed and compared for specimens manufactured with two materials, two machines with different process parameters, two build orientations, two surface conditions, and for sections with two different thicknesses. Based on the results of the conducted analysis, the following conclusions can be drawn:

1. The 3D analysis showed that the variability in defect distributions along the build height of 15 mm is not significant. However, defect distribution varies based on the location through the wall thickness of the specimens in as-built surface condition and concentration of more critical defects was observed closer to the inner and outer surfaces.
2. Distinct differences were observed between the distribution of defects in different quadrants of tubular Ti-6Al-4V AM250 specimens for both as-built and machined surface conditions. The build pattern, beam travel direction, location of the specimen on the platform, and proximity of the specimen to the rest of the specimens could influence the material/beam interactions and the distribution of the defects.
3. Optimization of the process parameters, surface machining, and HIP reduced the overall volume fraction of defects and the variability in defect distributions and created a more uniform and random dispersion of defects throughout the specimens. Duplicate HIPed specimens showed the best repeatability of the defect content.
4. In both diagonally and vertically built Ti-6Al-4V specimens, no variability in the distribution of defects across the wall thickness or around the specimens was observed after surface machining in case of well-optimized process parameters.

5. Defects of Ti-6Al-4V HIPed specimens did not show any directionality as opposed to the annealed specimens defects which were expanded perpendicular to the build direction. HIP reduced directionality in defects which results in less directional mechanical properties.
6. To represent AM defects more realistically for applications such as analysis of fatigue performance, the diameter, area, or volume as representations of defect size should be considered along with sphericity or aspect ratio which would affect the detrimental impact of the defect.
7. 2D analyses results showed equal or higher density of defects and larger defects in thicker grip section compared to thinner gage section for the same specimen which may have happened due to the differences in cooling rates and/or the variabilities in material/beam interactions.
8. Based on both 3D and high-resolution 2D analysis, aspect ratio and circularity/sphericity of the defects typically decrease as the defect diameter increases which make the larger defects more critical for fatigue performance.
9. 2D defect analysis with a sufficient number of cross-sections based on defect content could reveal trends similar to 3D analysis about the spatial distribution of defects. The 3D analysis provides much more details on the realistic morphology of the interconnected large LOF defects.
10. The 2D surface fraction of defects is closer to the 3D volume fraction of defects for specimens with a high density of small round defects; however, for specimens with a smaller number of defects and in the presence of LOF defects the difference between the surface fraction and volume fraction results becomes more significant.

Since fatigue is a local phenomenon and fatigue cracks usually start at stress concentrations, intrinsic AM defects are detrimental and play a key role in the fatigue performance of AM fabricated parts. The distribution of critical defects is important in quantifying the fatigue properties of AM parts. Analysis of characteristics of these process induced defects, as discussed in this paper, is the first step towards comprehending their impact on fatigue performance. Fatigue performance and probabilistic fatigue damage tolerant assessments of AM parts are the subjects of other publications by the authors.

CRediT authorship contribution statement

Niloofer Sanaei: Data curation, Formal analysis, Investigation, Visualization, Writing - original draft, Writing - review & editing. **Ali Fatemi:** Funding acquisition, Project administration, Resources, Supervision, Writing - review & editing. **Nam Phan:** Resources, Writing review & editing.

Acknowledgments

Financial support for this project was provided by NAVAIR. VGSTUDIO MAX 3.1 software license for this project was provided by Volume Graphics. The authors would like to thank Dr. Nima Shamsaei of Auburn University for fabricating most of the AM specimens. The authors would like to thank Brendan Lessel of NAVAIR for the micro-CT scans.

References

- [1] M. Seifi, M. Gorelik, J. Waller, N. Hrabec, N. Shamsaei, S. Daniewicz, J. Lewandowski, Progress towards metal additive manufacturing standardization to support qualification and certification, *JOM* 69 (3) (2017) 439–455.
- [2] A. du Plessis, S.G. le Roux, Standardized X-ray tomography testing of additively manufactured parts: a round robin test, *Addit. Manuf.* 24 (2018) 125–136.
- [3] T.M. Mower, M.J. Long, Mechanical behavior of additive manufactured, powder-bed laser-fused materials, *Mater. Sci. Eng. A* 651 (2016) 198–213.

- [4] G. Kasperovich, J. Hausmann, Improvement of fatigue resistance and ductility of TiAl6V4 processed by selective laser melting, *J. Mater. Process. Technol.* 220 (2015) 202–214.
- [5] H.K. Rafi, N.V. Karthik, H. Gong, T.L. Starr, B.E. Stucker, Microstructures and mechanical properties of Ti6Al4V parts fabricated by selective laser melting and electron beam melting, *J. Mater. Eng. Perform.* 22 (12) (2013) 3872–3883.
- [6] H.K. Rafi, T.L. Starr, B.E. Stucker, A comparison of the tensile, fatigue, and fracture behavior of Ti–6Al–4V and 15-5 PH stainless steel parts made by selective laser melting, *Int. J. Adv. Manuf. Technol.* 69 (5) (2013) 1299–1309.
- [7] M. Benedetti, V. Fontanari, M. Bandini, F. Zanini, S. Carmignato, Low- and high-cycle fatigue resistance of Ti–6Al–4V ELI additively manufactured via selective laser melting: mean stress and defect sensitivity, *Int. J. Fatigue* 107 (2018) 96–109.
- [8] S. Bagehorn, J. Wehr, H.J. Maier, Application of mechanical surface finishing processes for roughness reduction and fatigue improvement of additively manufactured Ti–6Al–4V parts, *Int. J. Fatigue* 102 (2017) 135–142.
- [9] N. Hrahe, T. Gnäupel-Herold, and T. Quinn, "Fatigue properties of a titanium alloy (Ti–6Al–4V) fabricated via electron beam melting (EBM): effects of internal defects and residual stress," *Int. J. Fatigue*, vol. 94, Part 2, pp. 202–210, 2017.
- [10] H. Gu, H. Gong, D. Pal, H. Rafi, T. Starr, B. Stucker, Influences of energy density on porosity and microstructure of selective laser melted 17-4PH stainless steel, *Conference: 24th Annual International Solid Freeform Fabrication Symposium*, 2013.
- [11] M. Seifi, A. Salem, D. Satko, J. Shaffer, and J. J. Lewandowski, "Defect distribution and microstructure heterogeneity effects on fracture resistance and fatigue behavior of EBM Ti–6Al–4V," *Int. J. Fatigue*, vol. 94, Part 2, pp. 263–287, 2017.
- [12] K.S. Chan, Roles of microstructure in fatigue crack initiation, *Int. J. Fatigue* 32 (9) (2010) 1428–1447.
- [13] A. Fatemi, R. Molaie, S. Sharifimehr, N. Phan, N. Shamsaei, Multiaxial fatigue behavior of wrought and additive manufactured Ti–6Al–4V including surface finish effect, *Int. J. Fatigue* 100 (2017) 347–366.
- [14] H.-W. Mindt, O. Desmaison, M. Megahed, A. Peralta, J. Neumann, Modeling of powder bed manufacturing defects, *J. Mater. Eng. Perform.* 27 (1) (2018) 32–43.
- [15] S.D. Zhang, J. Wu, W.B. Qi, J.Q. Wang, Effect of porosity defects on the long-term corrosion behaviour of Fe-based amorphous alloy coated mild steel, *Corros. Sci.* 110 (2016) 57–70.
- [16] J. Smith, W. Xiong, W. Yan, S. Lin, P. Cheng, O.L. Kafka, G.J. Wagner, J. Cao, W.K. Liu, Linking process, structure, property, and performance for metal-based additive manufacturing: computational approaches with experimental support, *Comput. Mech.* 57 (4) (2016) 583–610.
- [17] P. Edwards, M. Ramulu, Fatigue performance evaluation of selective laser melted Ti–6Al–4V, *Mater. Sci. Eng. A* 598 (2014) 327–337.
- [18] G. Kasperovich, J. Haubrich, J. Gussone, G. Requena, Correlation between porosity and processing parameters in TiAl6V4 produced by selective laser melting, *Mater. Des.* 105 (2016) 160–170.
- [19] S. Tammam-Williams, H. Zhao, F. Léonard, F. Derguti, I. Todd, P.B. Prangnell, XCT analysis of the influence of melt strategies on defect population in Ti–6Al–4V components manufactured by Selective Electron Beam Melting, *Mater. Charact.* 102 (2015) 47–61.
- [20] W. Xu, M. Brandt, S. Sun, J. Elambasseril, Q. Liu, K. Latham, K. Xia, M. Qian, Additive manufacturing of strong and ductile Ti–6Al–4V by selective laser melting via in situ martensite decomposition, *Acta Mater.* 85 (2015) 74–84.
- [21] V. Ben, K. Jean-Pierre, Selective laser melting of biocompatible metals for rapid manufacturing of medical parts, *Rapid Prototyp. J.* 13 (4) (2007) 196–203.
- [22] H. Gong, K. Rafi, H. Gu, G.D. Janaki Ram, T. Starr, B. Stucker, Influence of defects on mechanical properties of Ti–6Al–4V components produced by selective laser melting and electron beam melting, *Mater. Des.* 86 (2015) 545–554.
- [23] W.E. King, A.T. Anderson, R.M. Ferencz, N.E. Hodge, C. Kamath, S.A. Khairallah, A.M. Rubenchik, Laser powder bed fusion additive manufacturing of metals; physics, computational, and materials challenges, *Appl. Phys. Rev.* 2 (4) (2015) 041304.
- [24] S. Shao, M.J. Mahtabi, N. Shamsaei, S.M. Thompson, Solubility of argon in laser additive manufactured α -titanium under hot isostatic pressing condition, *Comput. Mater. Sci.* 131 (2017) 209–219.
- [25] J.J.S. Dilip, S. Zhang, C. Teng, K. Zeng, C. Robinson, D. Pal, B. Stucker, Influence of processing parameters on the evolution of melt pool, porosity, and microstructures in Ti–6Al–4V alloy parts fabricated by selective laser melting, *Progress in Additive Manufacturing* 2 (3) (2017) 157–167.
- [26] S. Leuders, M. Thöne, A. Riemer, T. Niendorf, T. Tröster, H.A. Richard, H.J. Maier, On the mechanical behaviour of titanium alloy TiAl6V4 manufactured by selective laser melting: fatigue resistance and crack growth performance, *Int. J. Fatigue* 48 (2013) 300–307.
- [27] S. Tammam-Williams, P.J. Withers, I. Todd, P.B. Prangnell, The effectiveness of hot isostatic pressing for closing porosity in titanium parts manufactured by selective electron beam melting, *Metall. Mater. Trans. A* 47 (5) (2016) 1939–1946.
- [28] W.W. Wits, S. Carmignato, F. Zanini, T.H.J. Vaneker, Porosity testing methods for the quality assessment of selective laser melted parts, *CIRP Ann. Manuf. Technol.* 65 (1) (2016) 201–204.
- [29] J.A. Slotwinski, E.J. Garboczi, K.M. Hebenstreit, Porosity measurements and analysis for metal additive manufacturing process control, *J. Res. Natl. Inst. Stand. Technol.* 119 (2014) 494–528.
- [30] A. du Plessis, I. Yadroitsev, I. Yadroitsava, S.G. Le Roux, X-ray microcomputed tomography in additive manufacturing: a review of the current technology and applications, *3D Print. Addit. Manuf.* 5 (2018).
- [31] C.A. Kantzos, R.W. Cunningham, V. Tari, A.D. Rollett, Characterization of metal additive manufacturing surfaces using synchrotron X-ray CT and micromechanical modeling, *Comput. Mech.* 61 (5) (2018) 575–580.
- [32] R. Molaie, A. Fatemi, N. Phan, Significance of hot isostatic pressing (HIP) on multiaxial deformation and fatigue behaviors of additive manufactured Ti–6Al–4V including build orientation and surface roughness effects, *Int. J. Fatigue* 117 (2018) 352–370.
- [33] ASTM-E2207-15, Standard practice for strain-controlled axial-torsional fatigue testing with thin-walled tubular specimens, *Annual Book of ASTM Standards*, vol. 03.01, 2015.
- [34] ASTM-B348-13, Standard specification for titanium and titanium alloy bars and billets, *Annual Book of ASTM Standards*, vol. 02, 2013, p. 04.
- [35] ASTM-F2924, Standard specification for additive manufacturing Titanium-6 Aluminum-4 Vanadium with powder bed fusion, *Annual Book of ASTM Standards*, vol. 10.04, 2014.
- [36] A. Fatemi, R. Molaie, J. Simsiriwong, N. Sanaei, J. Pegues, B. Torries, N. Phan, N. Shamsaei, Fatigue behaviour of additive manufactured materials: an overview of some recent experimental studies on Ti–6Al–4V considering various processing and loading direction effects, *Fatigue Fract. Eng. Mater. Struct.* 42 (5) (2019) 991–1009.
- [37] S. Tammam-Williams, P.J. Withers, I. Todd, P.B. Prangnell, The influence of porosity on fatigue crack initiation in additively manufactured titanium components, *Sci. Rep.* 7 (1) (2017) 7308.
- [38] I. Maskery, N.T. Aboulkhair, M.R. Corfield, C. Tuck, A.T. Clare, R.K. Leach, R.D. Wildman, I.A. Ashcroft, R.J.M. Hague, Quantification and characterisation of porosity in selectively laser melted Al–Si10–Mg using X-ray computed tomography, *Mater. Charact.* 111 (2016) 193–204.
- [39] A.B. Spierings, M. Schneider, R. Eggenberger, Comparison of density measurement techniques for additive manufactured metallic parts, *Rapid Prototyp. J.* 17 (5) (2011) 380–386.